Experimental Non-Equilibrium Radiation Measurements for Low-Earth Orbit Return

A.B. Glenn*, P.L. Collen†, and M. McGilvray‡
Osney Thermofluids Institute, University of Oxford, United Kingdom

This paper reports on absolute radiation measurements performed in synthetic air (20.78% O_2, 79.22% N_2) shock-heated flows. Experiments were carried out in the Oxford T6 Stalker Tunnel in Aluminium Shock Tube mode. Data is presented for velocities ranging from 5.5-7.2 km/s at a nominal 1 bar post-shock pressure, in both UV/Vis and Vis/NIR spectral ranges. Simulations of the equilibrium radiance using NASA CEA and NEQAIR codes underpredict that obtained from the experimental data. An analysis using the newly developed LASTA code removes shock deceleration from consideration as a cause for this discrepancy. Non-equilibrium data is analysed in the form of spectral and absolute non-equilibrium metrics, and the effects of shock speed and post-shock pressure on the non-equilibrium radiance isolated. Finite-rate one-dimensional two-temperature simulations using POSHAX3 with Park 1993 rates are performed, which significantly underpredict the experimentally acquired data.

I. Introduction

The thermochemical state of the excited species in the shock-layer ahead of an entry vehicle has a profound influence on heat transfer and aerodynamics around the vehicle. Excitation and relaxation of any of the translational, rotational, vibrational and electronic energy modes can result in radiation absorption and emission respectively. Quantum mechanics dictates that each energy mode can only exist at discrete levels, thus allowing only a finite number of discrete wavelengths that can be emitted from each species during bound-bound interactions. In an optically thin radiating medium, where absorption is negligible, the intensity of radiation at a specific wavelength is directly related to the number density of the species it originates from. Emission spectroscopy techniques can therefore be used to measure the number densities of species present in such a flow. Corrections are possible to account for the optical thickness in a flow with significant absorption. The rates of the thermochemical processes can also be inferred by observing the spatial or temporal variation of radiation intensity at wavelengths relevant to the species of interest. Radiation emission studies therefore not only reveal details of the radiative heating environment, but are essential to understanding the thermochemical state of the shock layer gas and the rates of processes in the non-equilibrium region.

Shock layer radiation emission studies for low-Earth orbit (LEO) return missions have received less attention than those for high-speed Lunar and Mars return missions in recent years, due to the low contribution of radiation to overall heating. The Space Shuttle trajectory is exemplary of such LEO return conditions, generally not exceeding velocities above 8 km/s. Radiative heating increases with velocity in an exponential fashion, only becoming significant relative to stagnation point convective heating at speeds above 10 km/s in air [1]. LEO returns have therefore not promoted study from a radiative heating standpoint. However, as previously addressed, radiation studies allow indirect investigation of the thermochemical state of the flow, which can help to overcome a number of engineering challenges. Aerothermodynamics is one such example: the coupling between the aerodynamic and thermal processes, which cause the forces on the surfaces of a vehicle to be affected by the thermochemical state of the gas around it. Heat transfer is also a strong motivator: though radiative heating may be negligible at LEO return conditions, the convective heating is largely influenced by the thermochemical state at the edge of the boundary layer. Observability is another example, for which radiation in the visible and infrared wavelength ranges are directly of interest. Finally, the onset of communications blackout occurs around 4 km/s due to the initial ionisation of molecules, producing free electrons capable of absorbing radio frequency radiation. These issues mentioned motivate further study into the radiating shock layer of LEO return vehicles, to provide a more detailed understanding of species present. This is achieved in this work via radiation emission measurements. At the conditions of interest in this paper, the non-equilibrium radiance exceeds that of the equilibrium region. The analysis discussed herein thus focuses on this region.

*DPhil Candidate, Department of Engineering Science, Oxford Thermofluids Institute, University of Oxford
†Postdoctoral Researcher, Department of Engineering Science, Oxford Thermofluids Institute, University of Oxford
‡Associate Professor, Oxford Thermofluids Institute, Department of Engineering Science, University of Oxford

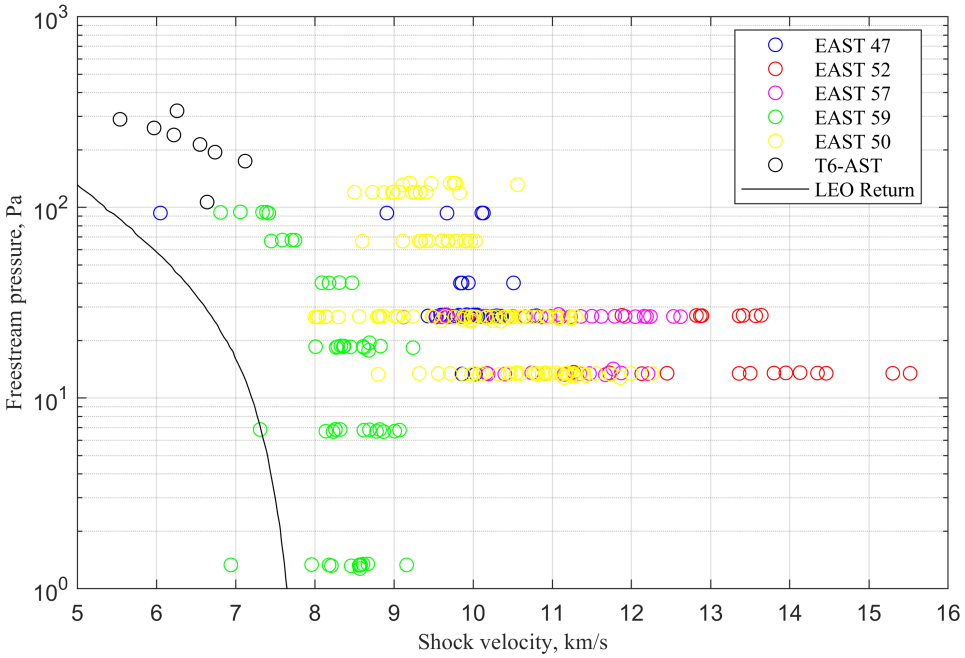

Fig. 1 T6 Aluminium Shock Tube test conditions studied in this paper compared against EAST test series in air and LEO return trajectory.

Non-equilibrium thermochemical relaxation phenomena and associated rate coefficients have been studied since the 1960s [2], though they are typically limited to high-velocity data and suffer from high uncertainties. Reducing uncertainties of non-equilibrium radiation has been identified as one of planet entry gas dynamics' highest priorities for the last 20 years [3]. Computational models capturing the non-equilibrium effects are still being developed and rely on experimental data for validation. In 2017, Cruden and Brandis [4] showed that current models don't predict non-equilibrium radiation accurately in air from 7–9 km/s due to the radiation being dominated by molecular non-equilibrium features, as opposed to atomic species which dominate at higher speeds [5–7]. Different aspects of the radiative and kinetic modelling are therefore being tested at these lower speed conditions. An extension of data to a wider combination of pressures and velocities will play an important role to improve the understanding of shock tube flows and their application to this low-speed regime.

This paper extends the Earth entry data available to lower velocities from 5.5 to 7.2 km/s, as shown in Fig. 1, plotted with a portion of a LEO return trajectory and air test series from the Electric Arc Shock Tube (EAST) [1] for reference. Most tests were undertaken at a post-shock pressure of 1 bar to enable future comparison to atmospheric plasma torch data. Tests were performed in the T6 Stalker Tunnel [8, 9] operating in Aluminium Shock Tube (AST) mode.

The experimental setup of the T6 facility in AST mode is described in Section II. Equilibrium data is compared to simulations using the NASA Chemical Equilibrium with Applications (CEA) in Section III. An analysis using the newly developed LASTA code is performed on two cases with different amounts of shock deceleration in Section IV. Finally, non-equilibrium data is analysed in Section V, and compared against predictions from a thermal and chemical relaxation solver. A number of different excitation models within the radiative modelling are compared for a nominal test case and the effects of shock velocity and post-shock pressure are assessed.

II. Experimental Setup

A. T6 Description

The T6 Stalker tunnel is a high enthalpy ground test facility at the University of Oxford, capable of reproducing atmospheric entry vehicle shock layer conditions. The facility has recently been described in detail by Collen et al. [8, 9]. Aluminium Shock Tube (AST) mode, illustrated in Fig. 2, was used for testing. Figure 3 is an image of the AST section, connected to the steel secondary driver on the left (upstream) and dump tank on the right (downstream).

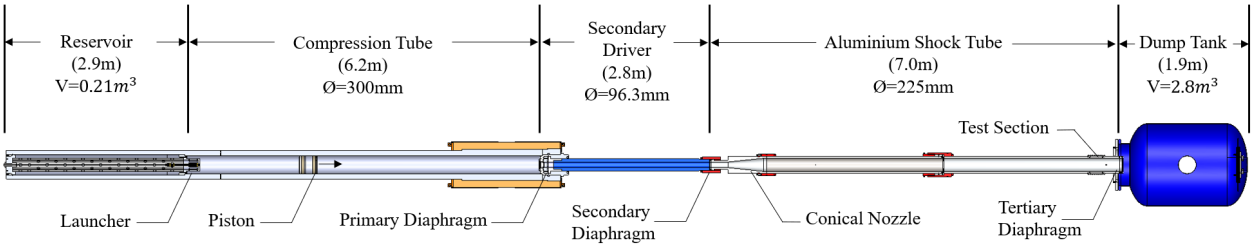

Fig. 2 Section view of T6 Stalker tunnel in Aluminium Shock Tube mode from above

Fig. 3 The T6 Aluminium Shock Tube, connected to the secondary driver (left) and dump tank (right)

The T6 facility utilises a free-piston driver, allowing for high shock speeds due to the generation of high sound speeds in the driver gas. The primary diaphragm initially separating the driver gas from the test gas is designed to rupture when a certain driver pressure is reached. This is controlled by diaphragm material, thickness and score depths. Reservoir air behind the piston is also filled to a set pressure, on the order of megapascals, specific to the tuned driver condition. To initiate a test, a vacuum pressure behind the piston is removed, allowing the high-pressure reservoir air to accelerate the piston through the compression tube, polytropically compressing the helium-argon mixture driver gas. The rapid increase in pressure causes the primary diaphragm to rupture, thus allowing expansion of the driver gas into the test gas, driving it downstream. Continued motion of the piston during this process delays expansion wave production by compressing the gas further.

Prior to this process, the AST section has been filled with a test gas to a pressure and composition relevant for the test case of interest. Upon primary diaphragm rupture, a normal shock wave is generated which progresses through this gas, compressing and accelerating it downstream. The flow between the normal shock and the contact surface (with the driver gas) is analogous to the stagnation streamline from the bow shock to the surface of an entry vehicle, travelling at the same speed as the shock and at an altitude with equivalent density as the initial shock tube fill. An optional secondary driver between the driver and AST can be filled with helium, by implementing a secondary diaphragm, to

reach faster shock speeds. In cases when it is not needed, there is no secondary diaphragm and the secondary driver is filled with the test gas. After the test gas passes the windows and enters the dump tank, a Pitot rake at the outlet of the tube is used to gather stagnation pressure and heat transfer data across the diameter of the test slug.

The design of the Aluminium Shock Tube lends itself to low-speed shock layer radiation studies. A conical nozzle section first increases the diameter from the nominal 96.3 mm secondary driver bore to 225 mm downstream. This provides a larger integration path-length for optically thin radiation, which is advantageous when capturing low-speed data due to the increased signal-to-noise ratio. In addition, the boundary layer formed around the tunnel circumference is relatively thinner compared to the tube diameter. This results in less shock deceleration and therefore longer test gas slugs [10], ideal for investigating the extent of non-equilibrium effects, as well as having a more uniform core flow. An optional tertiary diaphragm at the downstream end of the AST enables isolation of the test gas from the dump tank to reduce leak rates, though generally this was not needed during this experimental campaign. The aluminium construction is also advantageous as it reduces the presence of carbon contaminants in emission spectra. Finally, piezoelectric pressure transducers are located along the facility to measure the shock speed and static pressure.

Small doses of impurities in the test gas can have significant effects on the thermochemical reactions occurring in the test slug, thus causing the radiation captured from an experiment to deviate from the intended entry condition. Contaminants are therefore reduced by various means. Before filling the shock tube with the desired test gas, the initial atmospheric air is extracted via vacuum pumps. The tube is also flushed with the test gas multiple times to minimise the presence of remaining impurities. The ultimate pressure to achieve sufficient purity is dependent on the condition to be tested. In the synthetic air cases studied here, the fill pressures are relatively high and of similar composition to the real air evacuated, which further reduces uncertainties. For the data presented here, ultimate pressures of less than 1 Pa were achieved after flushing with the test gas, and leak rates less than 1 mPa s^{-1}. This was acceptable to avoid noticeable contamination in the majority of spectra for the test cases shown in this paper, with fill pressures all in excess of 100 Pa. Based on this ultimate pressure, leak rate and fill cycling, impurity percentages are estimated to be on the order of less than 1×10^{-7}% by volume. In addition to these attempts to reduce contaminants, the shock tube walls were cleaned with acetone before every test to remove traces of carbon from previous tests. In cases where contaminants are present, typically in the tail end of the equilibrium region, spectra have been averaged over regions which avoid their influence.

B. Test Conditions

The synthetic air test gas composition used for all tests was 20.78% O_2 and 79.22% N_2 by volume. A summary of the achieved conditions is provided in Table 1, data from which is plotted in Fig. 4. For each shot, a shock profile of the shock speed variation along the length of the tube is derived and uncertainties calculated following the method of James et al. [11]. The shock profiles for each test case are shown in Fig. 5. The first 3m are along the secondary driver, followed by the conical nozzle region, leading to the 225 mm diameter AST region which begins at 3.8m. The penultimate point on the trajectory is the velocity of the shock at the AST window. The measured post-shock pressures are determined from the pressure reading of the last shock timing station the shock passes at the window before the spatially and spectrally resolved image is taken.

Table 1 Summary of synthetic air conditions achieved in T6 Stalker tunnel. The shock speed that processed the test gas in the equilibrium and non-equilibrium regions at the time of emission spectroscopy camera gating are quoted separately.

Shot no.	P_{fill} (Pa)	$v_{Equilib}$ (km/s)	$v_{Non\text{-}equilib}$ (km/s)	$P_{2,Meas}$ (kPa)	$P_{2,CEA}$ (kPa)	$T_{2,CEA}$ (K)
195	290.0	5.66	5.54	99	99.7	6140
201	261.2	5.99	5.97	105	101.0	6346
194	240.0	6.26	6.22	98	101.6	6500
198	213.9	6.58	6.55	103	100.4	6666
196	195.0	6.87	6.74	100	100.0	6813
220	175.0	7.21	7.12	101	99.0	6983
207	106.7	6.64	6.64	50	51.1	6480
219	321.3	6.37	6.26	147	140.8	6663

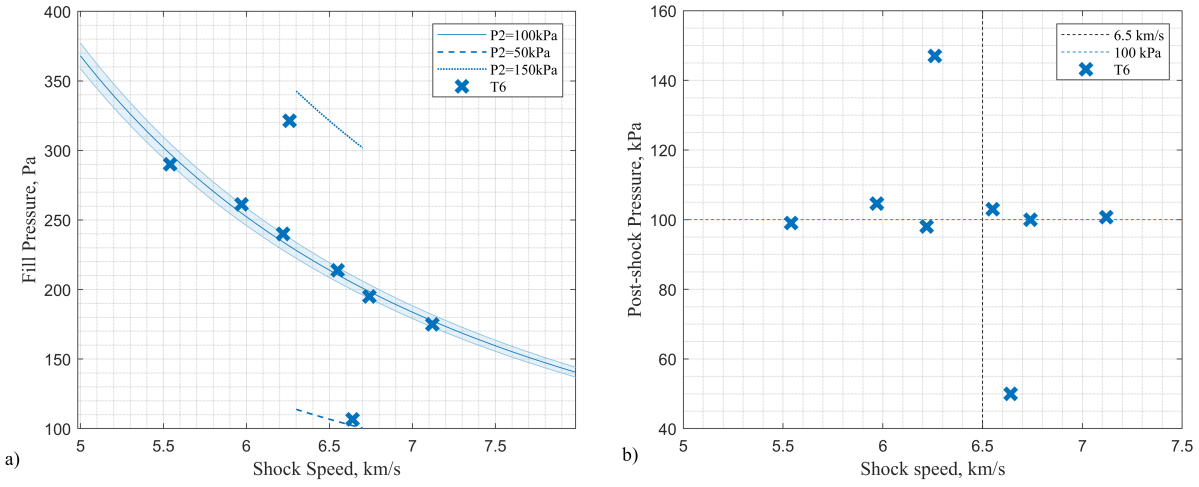

Fig. 4 Plots to illustrate synthetic air test conditions achieved: a) fill pressures used are compared to the theoretical values required to give a post-shock pressure of 1 bar for given shock speeds, shaded region indicates ±2.5 kPa; b) Post-shock pressure measured against shock speed.

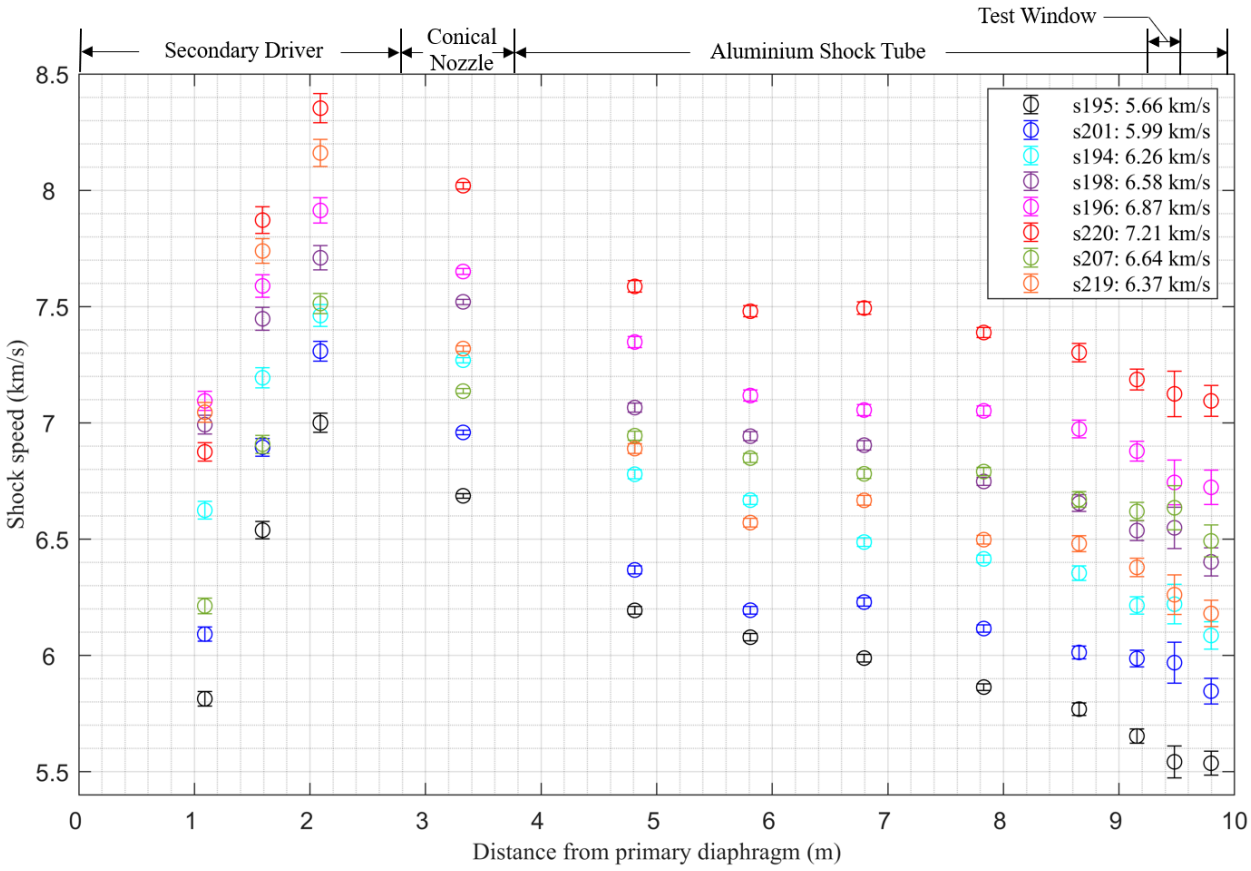

Fig. 5 Shock profile summary for the T6 AST synthetic air cases studied in this paper.

C. Optical Emission Spectroscopy (OES)

Primary analysis of the shocked gas is performed in the downstream section at the windows via two optical emission spectroscopy (OES) setups, as illustrated in Fig. 6. Radiation emitted from the test gas escapes through two 200 mm long, diametrically opposite windows along the tube axis. These are located 9.3 m from the primary diaphragm. Shock timing stations in this section are more closely spaced to provide higher resolution velocity measurement. Both windows have their own optical path and spectrometer, each with a designated wavelength region. For the synthetic air tests discussed here, a "blue side" is used to capture ultraviolet/visible wavelengths from 210 to 440 nm, and a "red side" for visible/near infrared from 600 to 840nm. The de-magnification factor of the red optical set up was 11.4. The blue side originally de-magnified by a factor of 25 but was then modified (due to a camera change part way through the campaign) to a factor of 20. Radiation along the length of the window is focused on the spectrometer slit; it is then spectrally separated by a diffraction grating while retaining its spatial profile along the tube axis. The wavelength dispersed image then falls on the camera sensor at the spectrometer outlet to finally capture the spatially and spectrally resolved image. Exposure times of 1µs or less are used to minimise smearing due to shock motion; this is especially important to analyse the transitory non-equilibrium region. On the red side, a Princeton Instruments Isoplane-320 spectrometer and Andor Intensified sCMOS camera were used, in a similar setup previously described by Collen et al. [12]. The blue side shown in Fig. 7 used a McPherson 218 0.3 m spectrometer and Princeton Instruments PIMAX:2 camera. An Andor iStar sCMOS 18U-E3 camera was also later used. Low resolution gratings, of 180 G/mm and 150 G/mm for the blue and red side respectively, were employed to provide access to broader wavelength ranges.

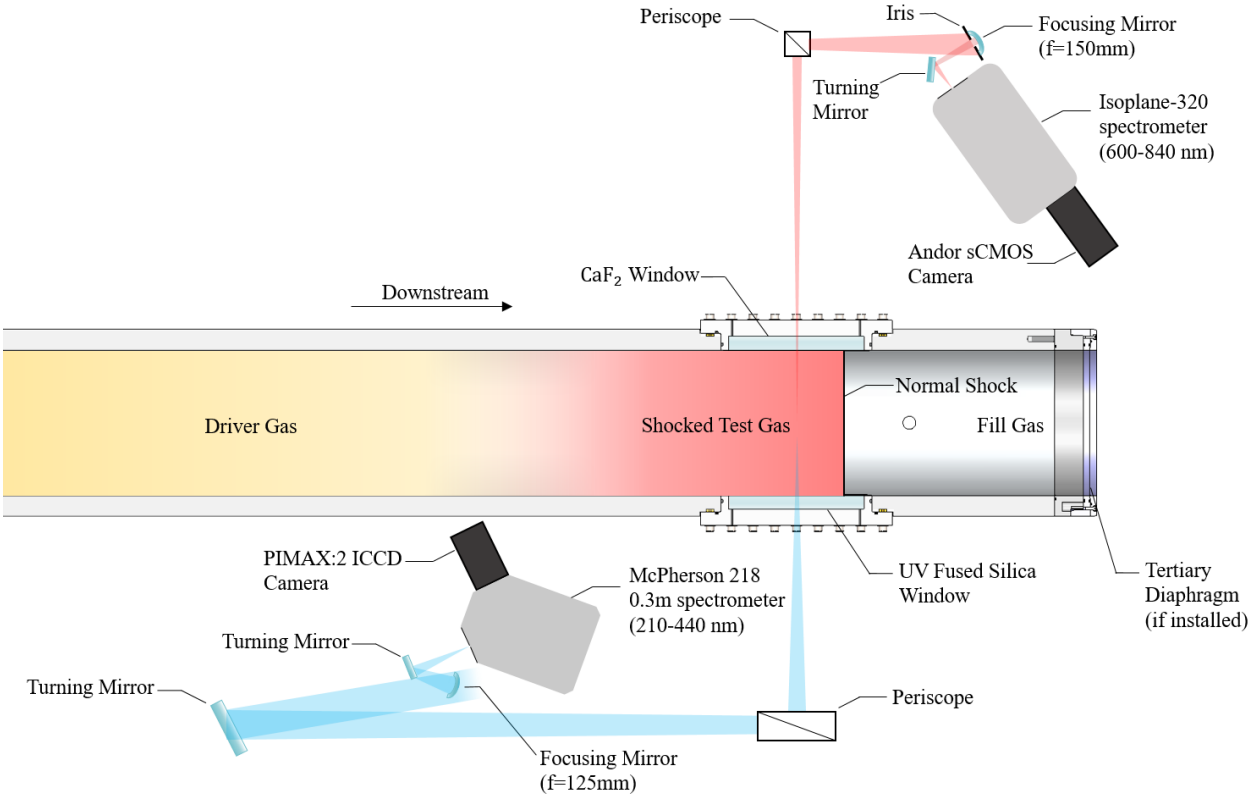

Fig. 6 The red (upper) and blue (lower) optical emission spectroscopy systems. Not to scale.

Calibrations were performed using a uniformly radiating integrating sphere, to produce a full field calibration at wavelengths above 300 nm for both the red and blue optical paths. In addition, a deuterium lamp is used to calibrate the blue side wavelengths below 300 nm. Calibrations were performed before every test. The procedure to calibrate shot data into units of spectral radiance has been described in detail by Collen [9] and is largely based on the methodology used at the Electirc Arc Shock Tube facility, as described by Cruden [1].

Fig. 7 Photo of the "blue side" optical setup to capture ultraviolet/visible radiation. An example image of the raw spatially and spectrally resolved data can be seen on the computer screen.

III. Equilibrium Data Validation

Radiative data from T6 AST experiments is obtained in the format of absolute radiance as a function of wavelength and position, as shown in Fig. 8 for an example in the Vis/NIR region. The vertical cross-section shows the radiance profile at a given wavelength. Data is integrated across the desired wavelength region to view the non-equilibrium peak at the shock front and relaxation to the subsequent equilibrium plateau. The horizontal cross-section gives spectral radiance at a given location. These are typically averaged over an appropriate portion of the equilibrium region to improve signal-to-noise ratio, while avoiding contaminated portions.

The equilibrium spectra and radiance profiles for shot 198 are displayed in Fig. 9, a condition with 6.55 km/s shock speed and 1 bar post shock pressure, accompanied by CEA-NEQAIR simulation results for comparison. The rest of the equilibrium data set for the remaining test cases is included in Appendix A. The simulations were run at the tunnel fill pressure and average shock speed from the three measurements before the shock reaches the window, as indicated in Fig. 5 and Table 1. This average speed is representative of the shock when it processed the gas that is in the equilibrium region at the time of OES camera gating. NEQAIR spectra have been convolved using the experimentally measured instrument line shapes (ILS) following the approach of Cruden [1].

It is clear that for both wavelength regions, in all test cases, the radiance from the experimental data exceeds that of the CEA-NEQAIR simulations. It is tempting to think this difference can be accounted for by subtracting a constant level of continuum background spectral radiance from the experimental data, to match CEA-NEQAIR predictions. If successful this would suggest the disagreement could be a result of excess electrons in the experiment due to shock deceleration or errors in the background subtraction method during data calibration. This method was trialled and though it does bring the baseline level radiation from the N_2 first positive band into close agreement, the height of the atomic peaks do not agree except for one or two fortuitous cases, suggesting excessive background emission in the core flow is not the issue. The study conducted in section IV also supports the conclusion that an excess of electrons from shock deceleration is not the cause of the increased radiation seen in the experiment. This is in agreement with the fact the shock profiles show relatively little deceleration and the radiance profiles generally have flat equilibrium plateaus, except where contaminants are present.

One possibility for the difference between experimental and simulated data is radiation originating from the boundary layer. When imaging the shock passing through the shock tube, the path length across the entire tunnel diameter is

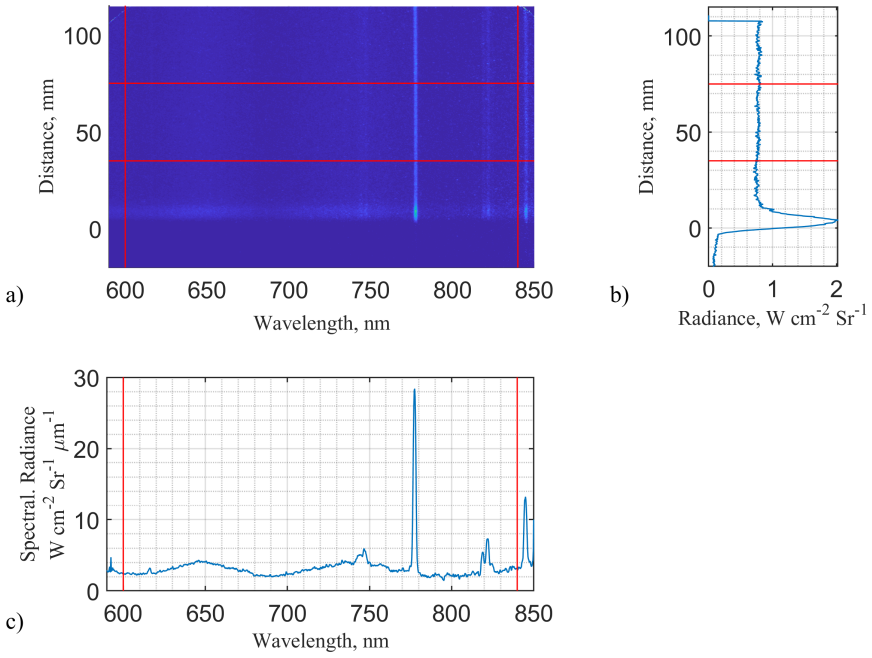

Fig. 8 Sample data set for Vis/NIR region, obtained in T6 facility from shot 198, 6.55 km/s, 103 kPa post-shock pressure. a) Absolute radiance as a function of position and wavelength is integrated between the vertical lines to obtain b) the radiance profile, while averaging between horizontal lines gives c) the equilibrium spectrum.

integrated, thus any radiation emanating from the boundary layer will be included in the analysed data. Viscous effects in the boundary layer may lead to higher temperatures, generating increased electron number densities and thus augmented continuum radiation. However, for the test cases considered here the boundary layer thickness is less than 1 mm in the equilibrium region of the test slug, thus contributing to less than 1% of the integration path length. Additionally, despite the regular cleaning of the internal tunnel walls, it is still likely that remnants on the surface will radiate when exposed to the high temperatures in the boundary layer or core flow.

Another possible source is the highly reflective aluminium tunnel walls. Radiation from the equilibrium region should be fairly constant and therefore reduce the effect of reflections, but the more intensely radiating non-equilibrium region could emit radiation which is subsequently reflected and superimposed on the equilibrium section of the flow. Additionally, stray light in the spectrometer could be contributing to the high radiation levels witnessed, though steps are taken at multiple points during the calibration procedure to rectify this effect via a “pedestal removal” technique [1]. Finally, radiative modelling errors within NEQAIR could be contributing to the observed discrepancies. These are low-speed conditions with significant radiation from molecular bands and therefore tests different aspects of the NEQAIR radiation modelling, compared to higher speed cases which are more dominated by atomic spectral lines.

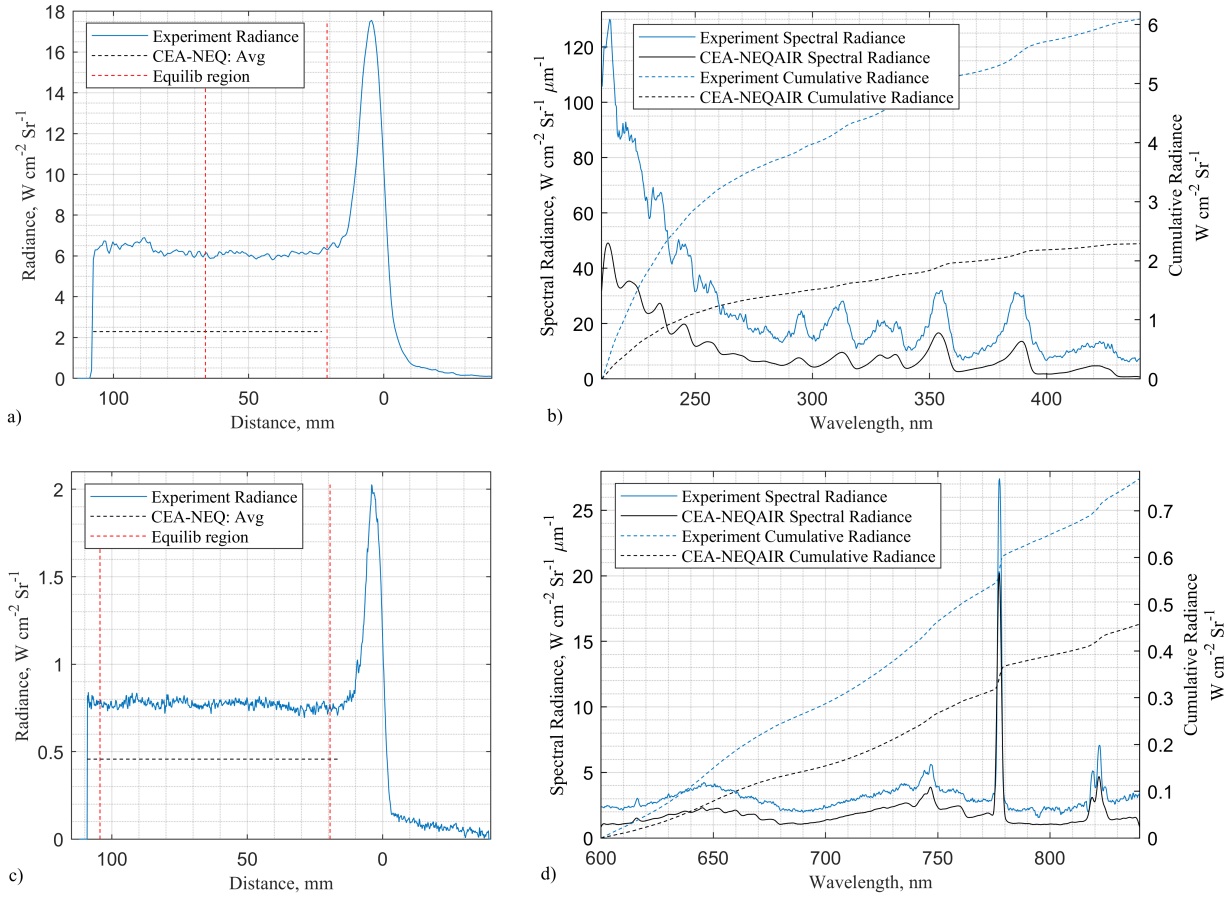

Fig. 9 Data summary for s198 at 6.55 km/s, 103 kPa post-shock pressure compared to CEA-NEQAIR simulations: a) radiance profile and b) equilibrium spectra for 210-440 nm; c) radiance profile and d) equilibrium spectra for 600-840 nm.

IV. LASTA Analysis

It has been demonstrated in the works of Satchell et al. [13–16] and Collen [9] that variations in shock speed down the tube and boundary layer growth cause variations in the test gas, which should be considered when analysing radiative data from shock tube experiments. A quasi one-dimensional Lagrange Shock Tube Analysys (LASTA) code has been developed at the University of Oxford to predict the variations in the test gas by discretising the test slug into a number of slices. The distance-time data of a given shock trajectory, along with test gas properties, fill pressure and tunnel dimensions are fed into the LASTA code to predict the compression and expansion waves required to induce the measured shock profile. The influence of those pressure waves on the thermochemical properties of each gas slice are calculated, providing a means to account for test-to-test variation in simulations by reconstructing the test slug of a given experiment.

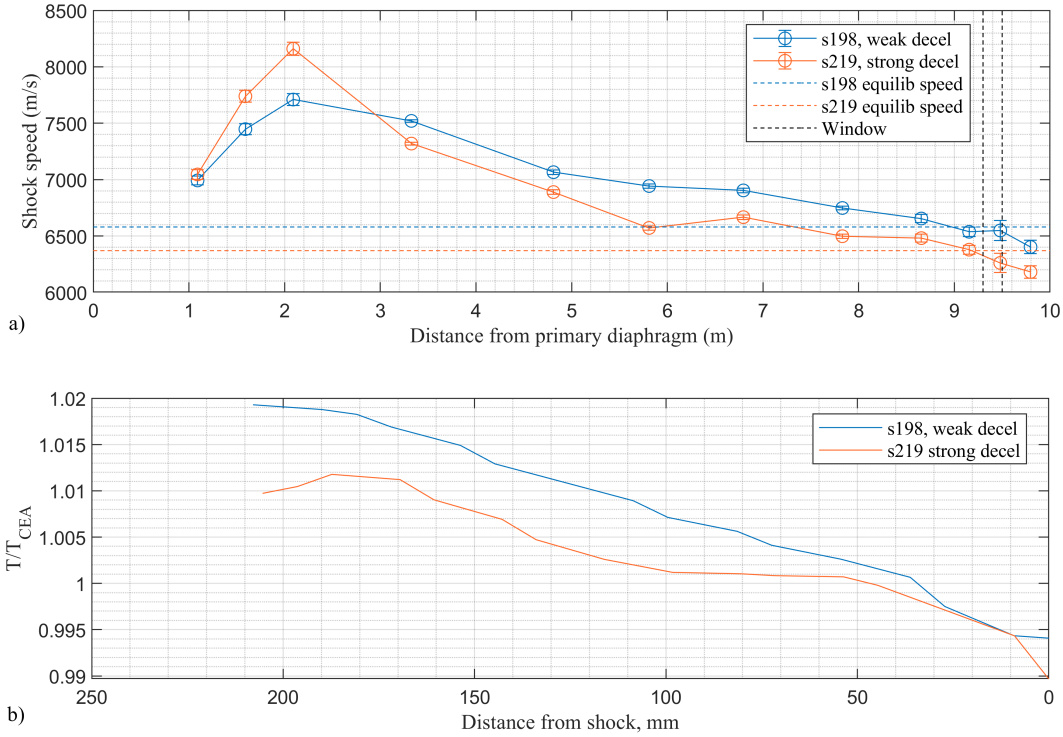

Fig. 10 Comparison of a) shock profiles and b) LASTA calculated temperatures normalised by CEA values through each test slug for two test cases with different amounts of shock deceleration.

To demonstrate the use of LASTA, two test cases are considered with different amounts of shock deceleration. The case with less shock deceleration is shot 198, which is compared to shot 219, having the greatest deceleration of all the test cases considered in this paper. The shock profiles are plotted in Fig. 10 a) with velocities used for the equilibrium CEA-NEQAIR simulations shown for reference. LASTA is able to calculate the properties of the core flow region in each slice. Figure 10 b) compares the temperatures calculated through the test slug of the two cases, each having been normalised by the equilibrium temperature calculated from CEA. Neither case significantly exceeds that of the equilibrium value calculated, with notable portions at the start of each test slug with temperatures less than the equilibrium values used, particularly for the case with more deceleration. This minor deviation from equilibrium through the test slug is likely due to the relatively small amounts of deceleration seen in each, in comparison to that typically seen for high-speed test cases.

The number densities of an 11-species model from the LASTA analysis were fed into NEQAIR to predict the radiance profiles of the two test cases. As can be seen in Fig. 11 and Fig. 12, the LASTA predictions are in very close agreement with that from CEA, with only very small gradients seen in the equilibrium region. LASTA only considers equilibrium conditions and so does not capture the non-equilibrium rise at the shock front. The close agreement between

the CEA and LASTA shock profiles eliminates excess electrons from shock deceleration as a potential cause of the increased level of background continuum radiation seen in the experimental data. This leaves reflections, boundary layer emission, background subtraction methodology during calibration and NEQAIR radiative modelling as potential sources of the discrepancy.

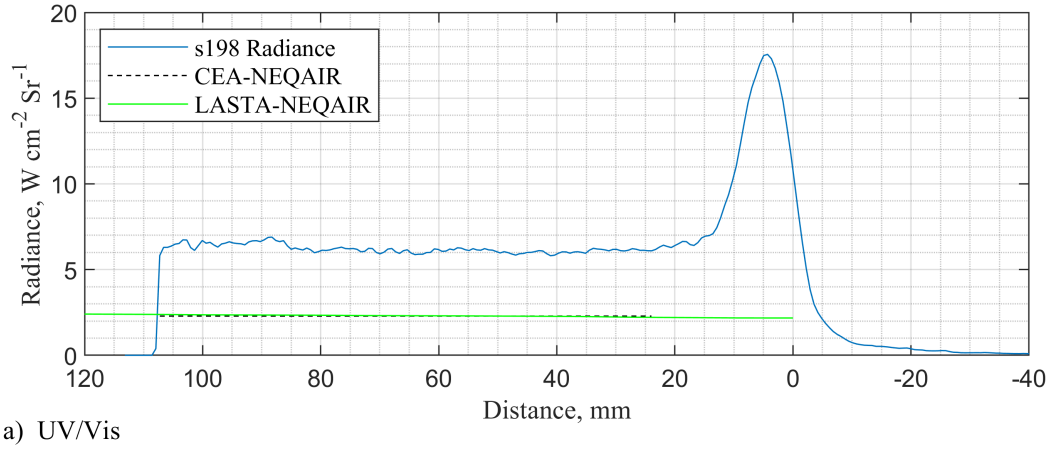

a) UV/Vis

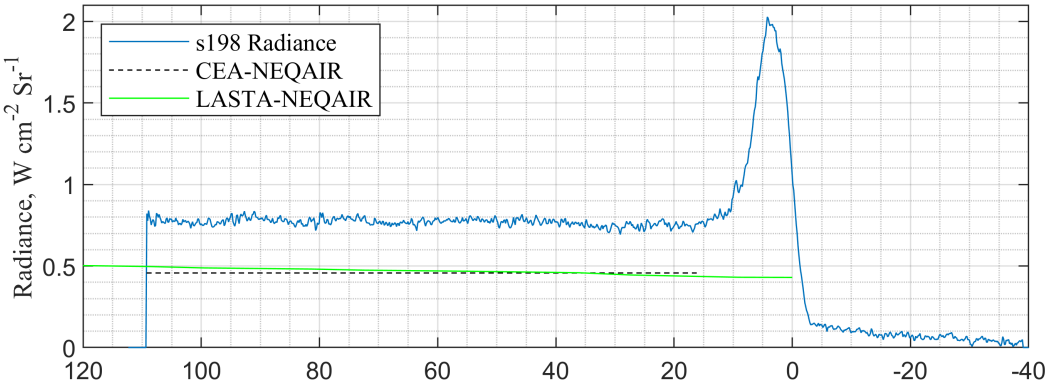

b) Vis/NIR

Fig. 11 Radiance profile comparisons between experiment, CEA, and LASTA for test case 198, for the a) UV/Vis (210-440 nm) and b) Vis/NIR (600-840 nm) region.

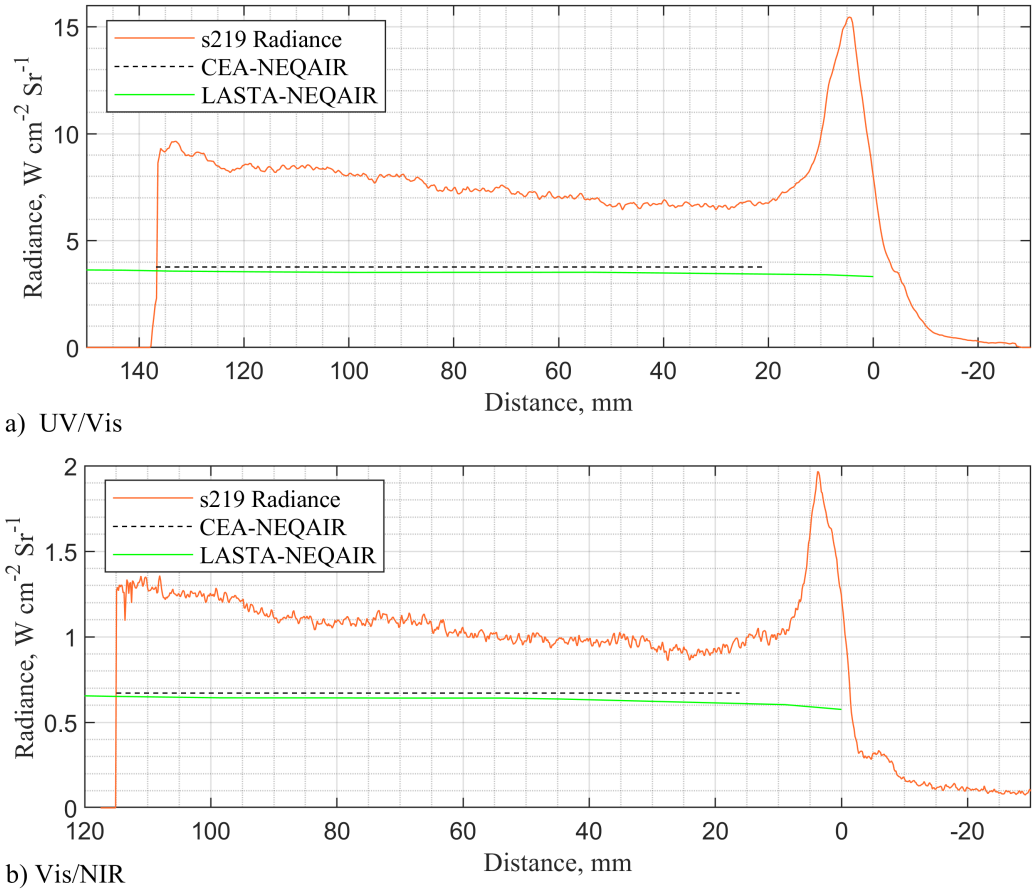

Fig. 12 Radiance profile comparisons between experiment, CEA, and LASTA for test case 219, for the a) UV/Vis (210-440 nm) and b) Vis/NIR (600-840 nm) region.

V. Non-Equilibrium Analysis

A. Modelling Process

To simulate the non-equilibrium region of the given test cases, a finite-rate one-dimensional thermal and chemical relaxation solver (POSHAX3) [17], developed at the University of Queensland, with an 11-species two-temperature air model with Park 1993 [2] reaction rates is used. The inputs required are shock speed, initial temperature, pressure and composition, in addition to the selection of appropriate chemical reaction and energy exchange rates. The shock speed at the window is used as the input for these simulations since that is the closest reading available to the speed of the shock when it processed the test gas in the non-equilibrium region at the time of OES camera gating. Results from the POSHAX simulations are fed into the NASA NEQAIR code to predict the corresponding radiance profiles for each wavelength region. The ILS and Spatial Resolution Functions (SRF), measured during the wavelength and spatial calibrations respectively, are convolved into the NEQAIR simulations to account for the broadening mechanisms imposed on the experimental data, enabling a like-for-like comparison between the two.

An example comparison between the experimentally measured and POSHAX3-NEQAIR radiance profiles is given in Fig. 13 for test 198. It is encouraging to see that the equilibrium plateaus from the POSHAX3 simulations overlie with the CEA simulations also run with the shock speed at the window, suggesting the final thermochemical state arrived at by POSHAX3 is correct. However, it is evident that the result from NEQAIR simulations underpredicts the experimentally measured radiance profiles, especially in the UV/Vis region. Hence, the species predicted in the non-equilibrium region by the Park 93 two-temperature model do not agree with the profile captured in the experiment. Future works will extend this by implementing other kinetic and radiative models.

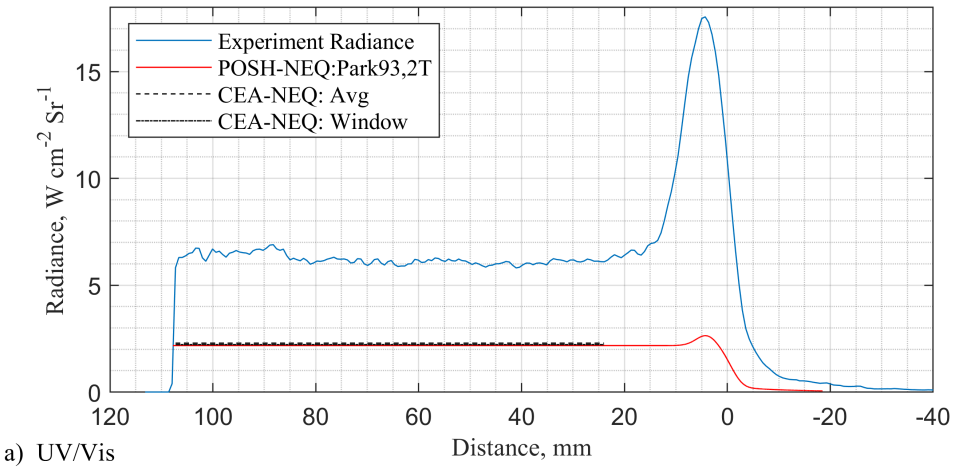

Fig. 13 Radiance profile comparisons between experiment, CEA, and POSHAX3 using Park 93 rates and a two-temperature model for test case 198, for the a) UV/Vis (210-440 nm) and b) Vis/NIR (600-840 nm) region.

B. Non-Equilibrium Metrics

Non-equilibrium data in previous work by Cruden et al. [4] [18, 19] has been analysed in terms of spectral and absolute non-equilibrium metrics (NEMs), providing a means to summarise and compare a number of simulations and experimental results while still maintaining a physically relevant meaning. The spectral NEM is defined as the average radiance within ±20 mm of the peak radiance, giving a result as a function of wavelength, as shown in equation 1 (where L is the spectral radiance, W cm^{-2} sr^{-1} µm^{-1}). The absolute NEM is the integrated radiance of the spectral NEM, as shown in equation 2.

$$NEM_{\text{spec}}(\lambda) = \frac{1}{D_{\text{tube}}} \int_{y_{\text{pk}}-20}^{y_{\text{pk}}+20} L(y,\lambda)\, dy \tag{1}$$

$$NEM_{\text{abs}} = \frac{1}{D_{\text{tube}}} \int_{\lambda_{\text{low}}}^{\lambda_{\text{high}}} \int_{y_{\text{pk}}-20}^{y_{\text{pk}}+20} L(y,\lambda)\, dy\, d\lambda \tag{2}$$

An illustration of the ±20 mm region centered on the peak radiance is illustrated in Fig. 14. These metrics capture the non-equilibrium peak and are long enough to contain the camera and optical smearing functions, enabling comparison of data between tests with different values of these experimental parameters. The experimentally obtained spectral non-equilibrium metrics for each test case are included in the data summary of Appendix A, along with summary plots in Appendix B to aid comparison between test cases.

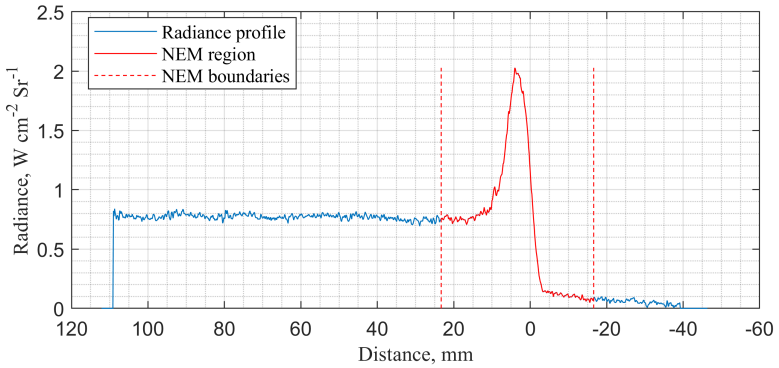

Fig. 14 Illustration of the region integrated for the non-equilibrium metrics, ±20 mm of the peak radiance, for the Vis/NIR region of test case 198.

C. Results

The absolute NEM values for the 1 bar post-shock test cases are plotted against shock speed in Fig. 15 and Fig. 16 for the UV/Vis and Vis/NIR regions respectively. These are compared to the results of the POSHAX3-NEQAIR simulations, corresponding radiance profiles for which are included in Appendix A. In the Vis/NIR region, the experimental data displays an exponential increase in non-equilibrium radiance with shock speed. This trend seems to be captured by the POSHAX3-NEQAIR simulations, though is significantly underpredicted (60 to 70%) at the cases available for comparison. The absolute NEM for the 1 bar post-shock experimental data of the UV/Vis region also increases with shock speed and is generally one order of magnitude greater than the Vis/NIR region. The trend exhibits a more asymptotic increase with velocity, as opposed to exponential, with a sudden drop after around 6.6 km/s corresponding to the decrease in spectral NEM from the NO region (see Fig. 35 in Appendix B). The NO species radiating from 200 to 300 nm are the most intensely radiating species of both the wavelength regions considered in this paper and hence have a noticeable effect when their dissociation rates increase to reduce their number densities. Further numerical simulations and repeated testing of this regime will help to assess the legitimacy of this decrease. Thereafter, the absolute NEM continues to increase as the effects of increasing velocity outweigh the reducing NO number densities. The POSHAX3-NEQAIR simulations underpredict the UV/Vis absolute NEM values by 70-80% in this region, again demonstrating inaccurate capturing of the thermochemical state in the non-equilibrium region at these conditions.

Figure 17 and Fig. 18 display the absolute NEM as a function of post-shock pressure between cases with similar shock speeds for the UV/Vis and Vis/NIR regions respectively. POSHAX3-NEQAIR comparisons are once again

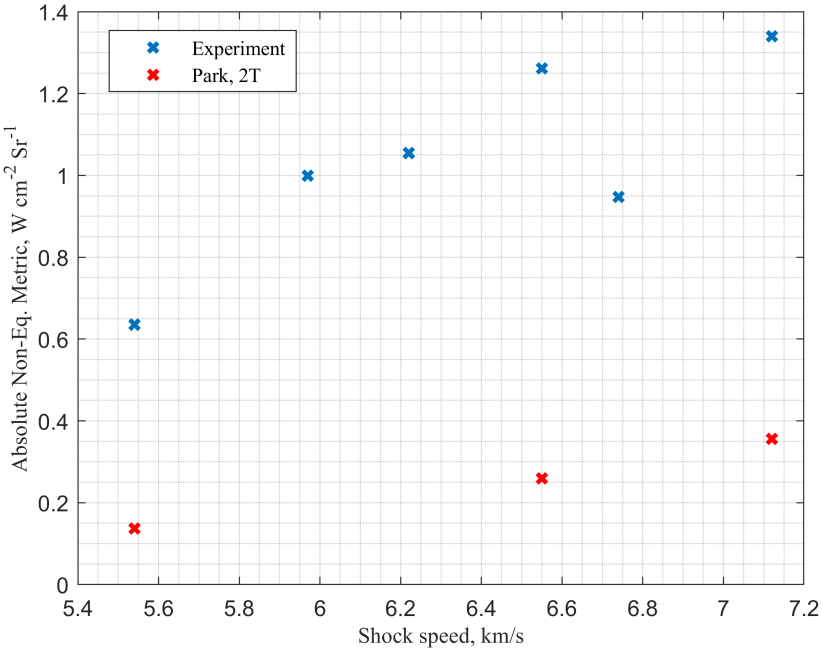

Fig. 15 Summary of absolute NEM values versus shock speed from 210 to 440 nm, at 1 bar post-shock pressure. POSHAX3-NEQAIR simulation results from a two-temperature model using Park 1993 rates are shown for comparison at nominal and extreme conditions.

provided for comparison, plotted with the final post-shock pressures calculated from the POSHAX3 simulation. The increase in absolute NEM appears to be asymptotic with increase in post-shock pressure for both wavelength regions, except for the high-pressure case in the UV/Vis region where a drop in absolute NEM occurs. The asymptotic trend can be explained by the increasing number of molecules and atoms radiating as the pressure and therefore density in the radiating region increases. The absolute NEM of test case 198 is nearly double that of 207, corresponding to the increase from 0.5 to 1 bar post-shock pressure. Deviations from this trend, including the drop in the UV/Vis for the high-pressure test case, are believed to be a result of the shock speeds decreasing for each increase in post-shock pressure, preventing a true like-for-like comparison between the test cases. In addition, there could be an increase in optical thickness with post-shock pressure, reducing the measured radiation. The POSHAX3-NEQAIR simulations capture the asymptotic trend well for both wavelength regions however significantly underpredict the experiment data, by 55-60% for the Vis/NIR region and 70-85% for the UV/Vis region.

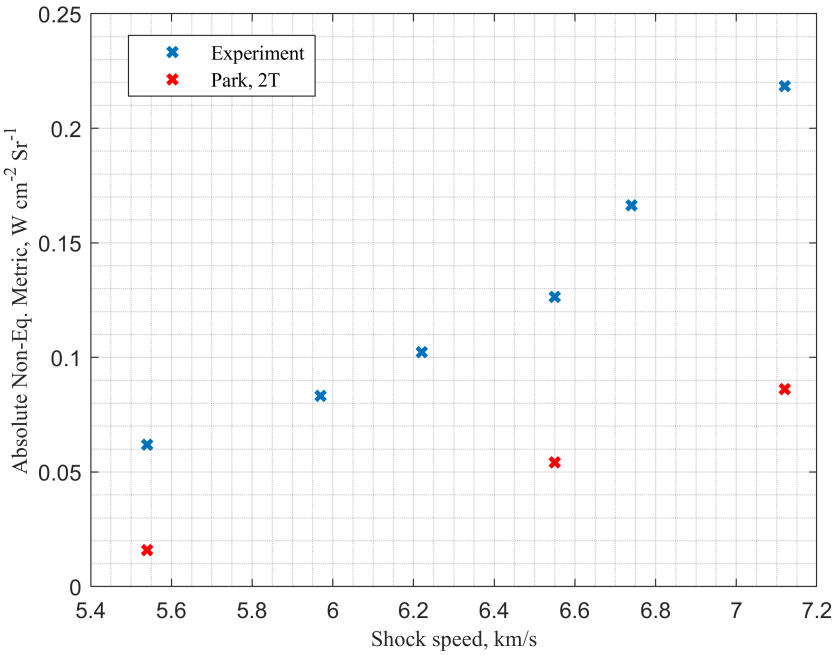

Fig. 16 Summary of absolute NEM values versus shock speed from 600 to 840 nm, at 1 bar post-shock pressure. POSHAX3-NEQAIR simulation results from a two-temperature model using Park 1993 rates are shown for comparison at nominal and extreme conditions.

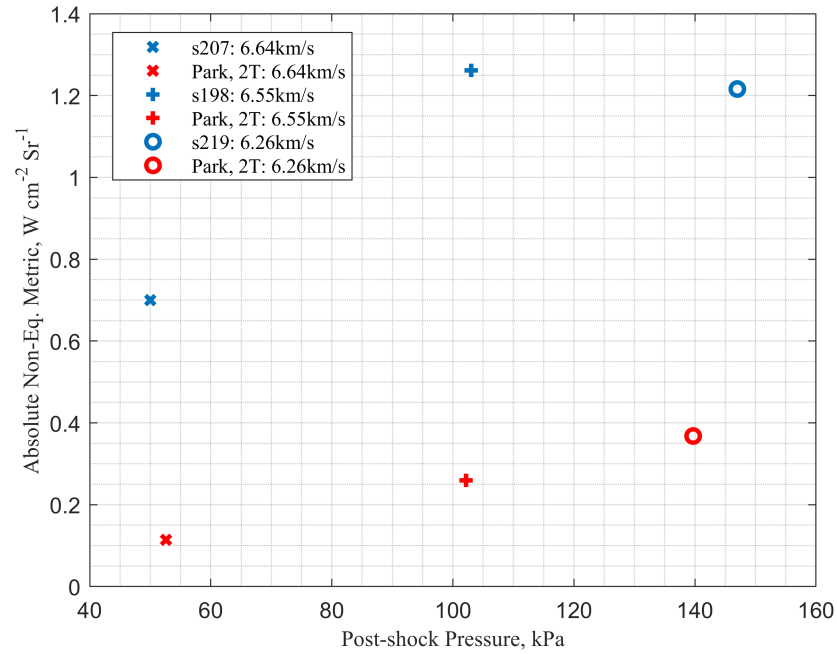

Fig. 17 Summary of absolute NEM values versus post-shock pressure from 210 to 440 nm. POSHAX3-NEQAIR simulation results from a two-temperature model using Park 1993 rates are shown for comparison.

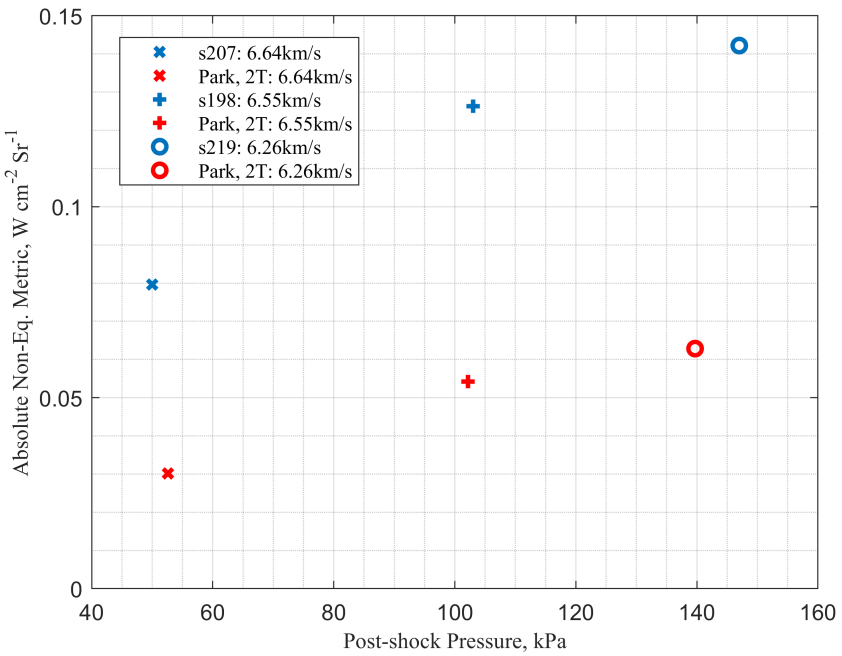

Fig. 18 Summary of absolute NEM values versus post-shock pressure from 600 to 840 nm. POSHAX3-NEQAIR simulation results from a two-temperature model using Park 1993 rates are shown for comparison.

D. Alternative Excitation Models

The radiative simulations up to now have been carried out using the non-Boltzmann rates in NEQAIR version 15.0. The nominal test case (shot 198) with 6.55 km/s shock speed at the window and 1 bar post-shock pressure, is chosen to perform a preliminary comparison of predicted absolute NEM values against a range of excitation rates, including the recently updated NEQAIR version 15.1. Table 2 compares the results of the two codes, as well as the effect of implementing alternative excitation models. The molecular excitation rates recently attained from Cruden and Brandis [4] for 7-9 km/s air shocks are compared against models using the atomic excitation rates of Huo et al. [20] and the traditional rates from Park 1990 [21]. The results predominantly underpredict the experimentally obtained absolute NEM values quite significantly, with the exception of the Cruden and Brandis molecular excitation rates in the Vis/NIR region which overpredicts considerably. The results of the Vis/NIR region show the most sensitivity to excitation model selection. All simulations relax to the same equilibrium radiance, which has been shown to underpredict the experimentally observed equilibrium radiance. This will have some effect on the predicted NEM values by inherently reducing the area in the relaxation region behind the peak. It should be noted that all kinetic modelling here has been performed using the same two-temperature model with Park 1993 rates via the POSHAX3 simulations. At the time of writing, it is too early to assess which excitation model is best for these test conditions. These analyses will continue by testing a wide range of combinations of radiative and kinetic modelling options, with the ultimate goal of extracting the rates of the thermochemical processes during the relaxation phase.

Table 2 Comparison of absolute NEM predictions from different NEQAIR excitation rate models, all performed using the two-temperature Park 1993 kinetic model, for the nominal test case 198.

NEQAIR Ver.	Model	ref	210-440nm		600-840nm	
			Abs NEM, W cm^{-2} sr^{-1}	% of Exp.	Abs NEM, W cm^{-2} sr^{-1}	% of Exp.
15.0	Default	-	0.259875	20.6	0.054213	42.9
15.1	Default	-	0.327879	26.0	0.078113	61.8
15.1	Cruden	[4]	0.305800	24.2	0.176682	139.8
15.1	Huo	[20]	0.327787	26.0	0.075196	59.5
15.1	Park	[21]	0.328082	26.0	0.083127	65.8

VI. Conclusion

Experiments of LEO return shock speeds in synthetic air have been carried out in the T6 Stalker Tunnel operating in Aluminium Shock Tube mode. Both equilibrium and non-equilbrium data from these tests have been analysed. Simulations using NASA CEA-NEQAIR codes underpredict the spectral radiance of all low-speed test cases considered. An analysis using the newly developed LASTA code for two cases with different amounts of shock deceleration has demonstrated the deceleration to have negligible effect on predicted equilibrium radiance for the cases considered, due to the minimal deceleration seen in these low-speed tests. This conclusion leaves boundary layer effects, reflections from the internal tunnel wall, the experimental background subtraction methodology and radiative modelling within NEQAIR as potential causes for the disagreement between the two data sets.

The presented absolute NEM data has shown revealed radiance from the non-equilibrium region increases exponentially with velocity in the Vis/NIR region and asymptotically in the UV/Vis, with increasing NO dissociation becoming significant from around 6.6 km/s. The post-shock pressure experienced by the radiating molecules increases non-equilibrium radiance in an asymptotic fashion, due to the increased density of radiating atoms and molecules. There is also likely an increase in optical thickness with post-shock pressure, which could influence the measurement. Comparisons made using a finite-rate one-dimensional two-temperature model with Park 1993 rates in POSHAX3 show significant underprediction of the experimental data captured, by up to 80%. A preliminary comparison of results using different excitation models within NEQAIR for a nominal test case brings simulation closer to experiment in some cases though still generally underpredicts.

These analyses will continue by comparing the equilibrium 1 bar data against equivalent conditions from the Ecole Centrale radio-frequency TAFA Model 66 ICP Torch. This approach will help to identify the source of discrepancies seen in the equilibrium data. The investigation of alternative radiative and kinetic models to simulate the non-equilibrium data will be continued. The ultimate intention for this data is to extract rates of the thermochemical processes occurring in the non-equilibrium region for these LEO return speeds. Finally, this work has presented a new experimental dataset relevant to the shock layer of LEO return conditions. This compliments and extends existing results in the literature, and can now be used to aid development and validation of numerical tests. Work in these areas is on-going.

Appendix

Experimental and simulated data for all test cases considered in this study is presented in the following figures. Section A gives a summary of the experimental equilibrium and non-equilibrium data for each test case, along with results from simulations, thus providing the information to investigate and assess each test case individually. Sections B, C and D provide a summary of all the experimental data across all cases to aid their comparison. The figures are plotted according to post-shock pressures and wavelength regions.

A. Test Case Summaries

The data presented in the figures of this section gives a summary of shock profiles, radiance profiles, equilibrium spectra and measured spectral NEM for both the UV/Vis (210-440 nm) and Vis/NIR (600-840 nm) wavelength ranges, for each individual test case. Simulations using CEA-NEQAIR and POSHAX3-NEQAIR, when relevant, are included for comparison in the figures.

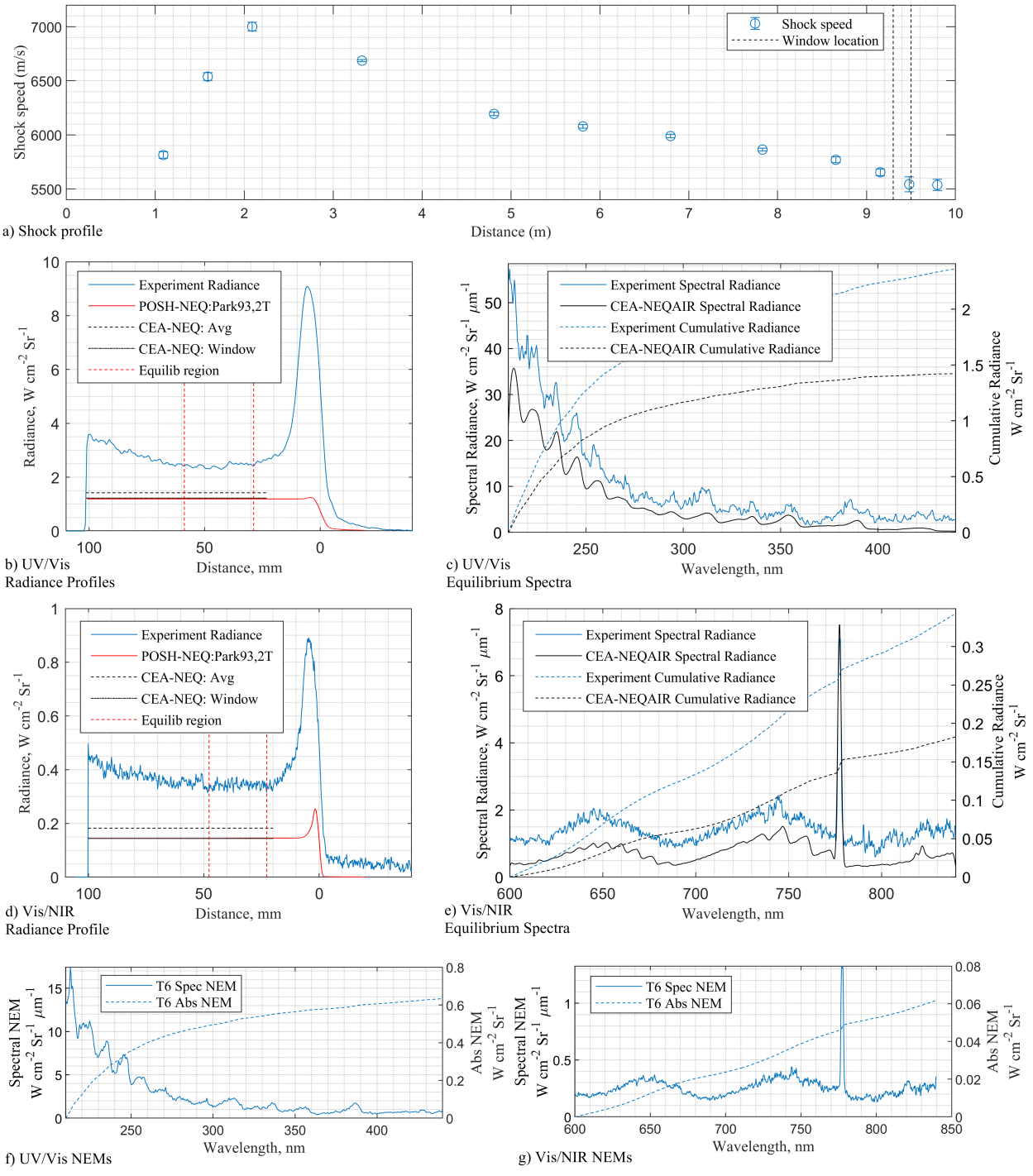

Fig. 19 Data summary for s195 at 5.66 km/s, 99 kPa post-shock pressure compared to simulations. a) shock profile; b) radiance profile and c) equilibrium spectra for UV/Vis (210-440 nm); d) radiance profile and e) equilibrium spectra for Vis/NIR (600-840 nm); measured non-equilibrium metrics for f) UV/Vis and g) Vis/NIR.

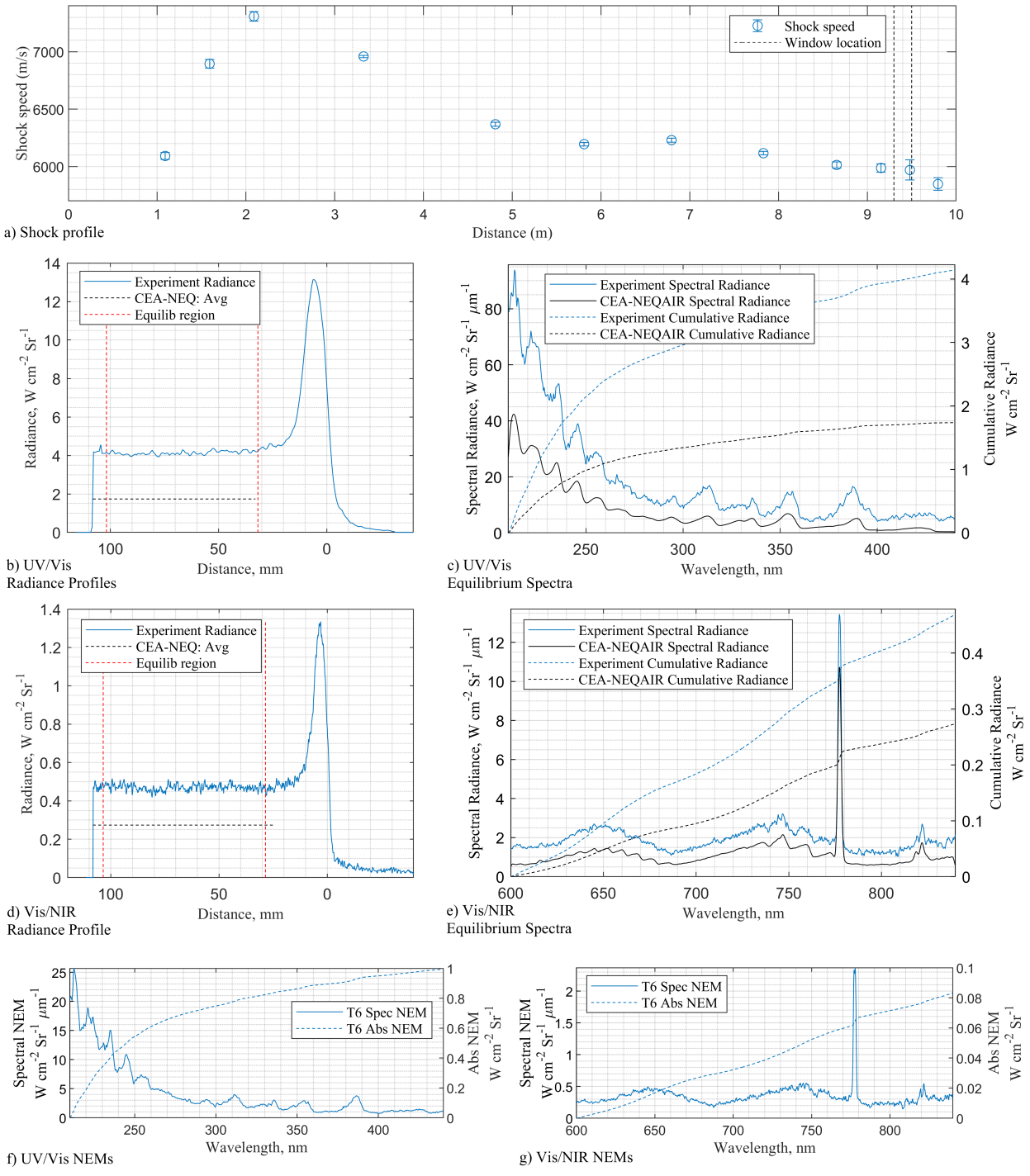

Fig. 20 Data summary for s201 at 5.99 km/s, 105 kPa post-shock pressure compared to simulations. a) shock profile; b) radiance profile and c) equilibrium spectra for UV/Vis (210-440 nm); d) radiance profile and e) equilibrium spectra for Vis/NIR (600-840 nm); measured non-equilibrium metrics for f) UV/Vis and g) Vis/NIR.

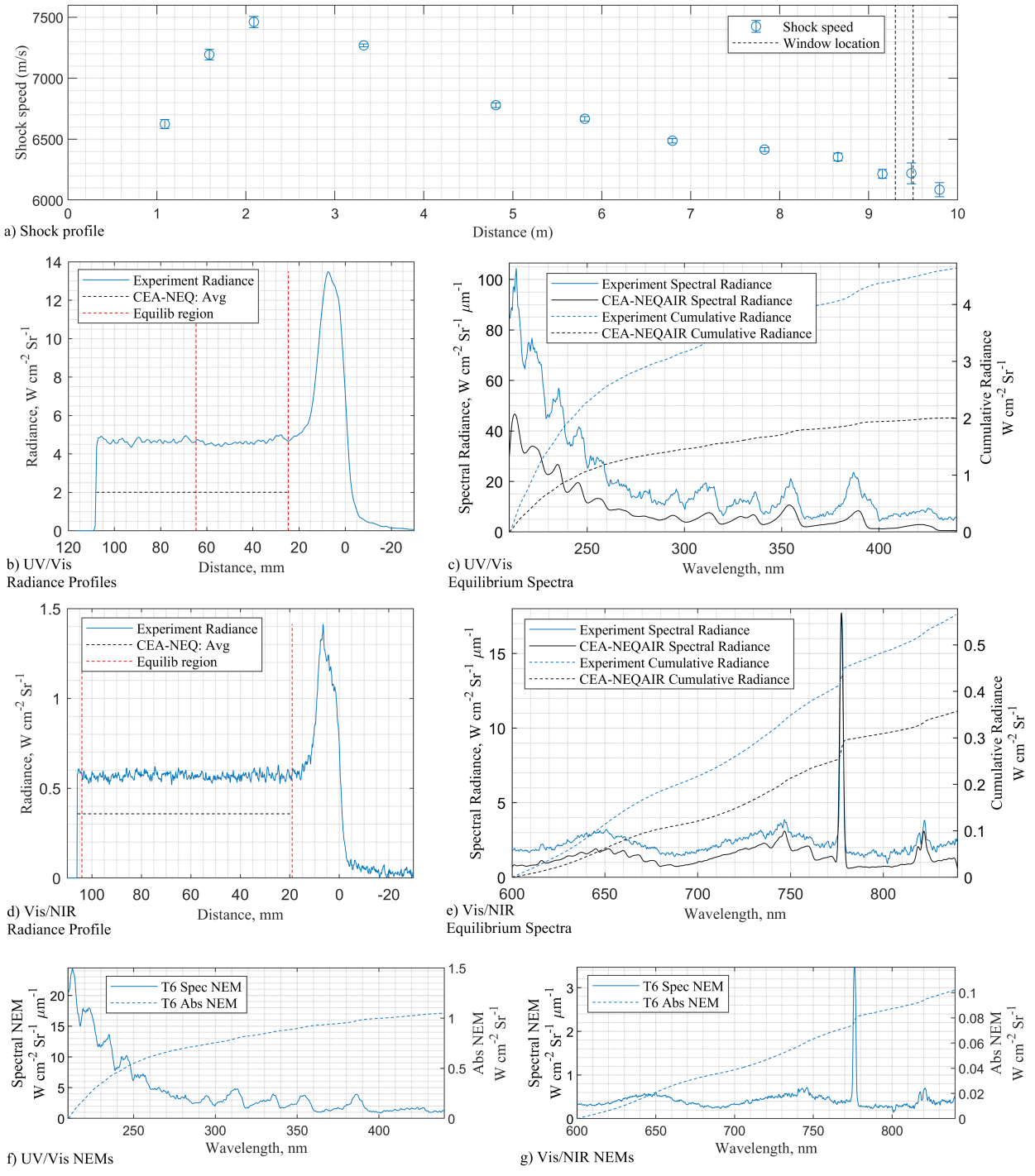

Fig. 21 Data summary for s194 at 6.26 km/s, 98 kPa post-shock pressure compared to simulations. a) shock profile; b) radiance profile and c) equilibrium spectra for UV/Vis (210-440 nm); d) radiance profile and e) equilibrium spectra for Vis/NIR (600-840 nm); measured non-equilibrium metrics for f) UV/Vis and g) Vis/NIR.

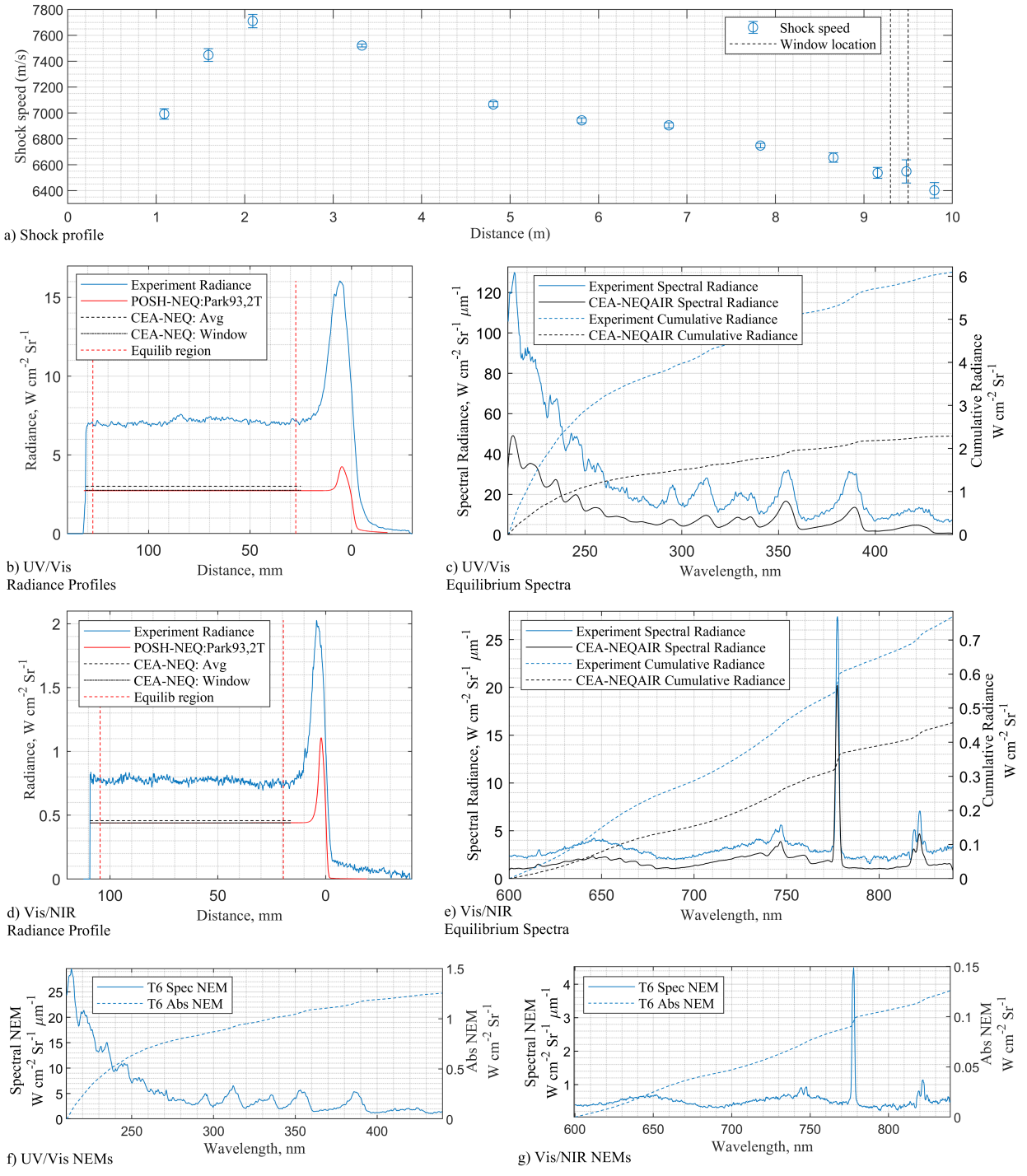

Fig. 22 Data summary for s198 at 6.58 km/s, 103 kPa post-shock pressure compared to simulations. a) shock profile; b) radiance profile and c) equilibrium spectra for UV/Vis (210-440 nm); d) radiance profile and e) equilibrium spectra for Vis/NIR (600-840 nm); measured non-equilibrium metrics for f) UV/Vis and g) Vis/NIR.

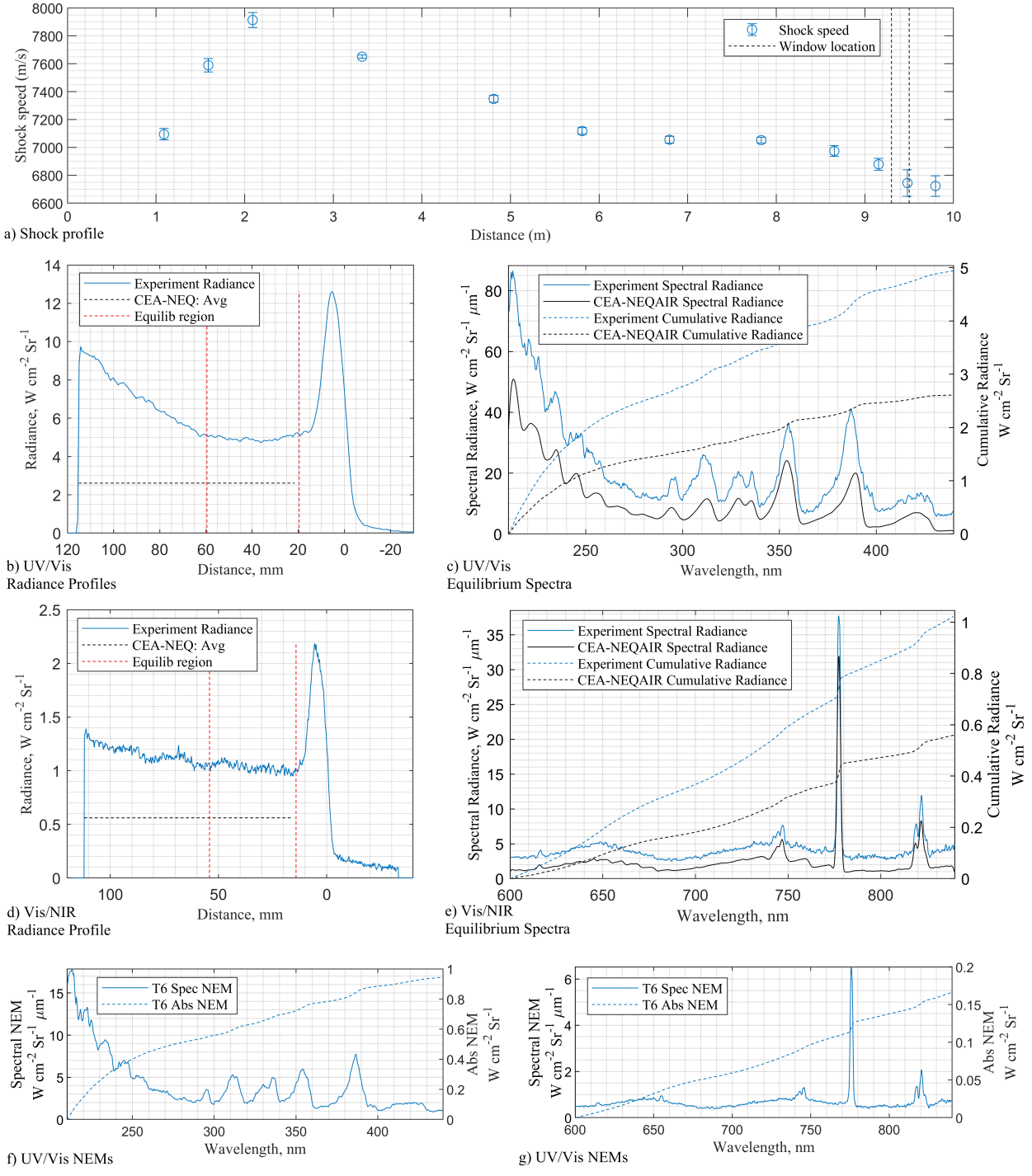

Fig. 23 Data summary for s196 at 6.87 km/s, 100 kPa post-shock pressure compared to simulations. a) shock profile; b) radiance profile and c) equilibrium spectra for UV/Vis (210-440 nm); d) radiance profile and e) equilibrium spectra for Vis/NIR (600-840 nm); measured non-equilibrium metrics for f) UV/Vis and g) Vis/NIR.

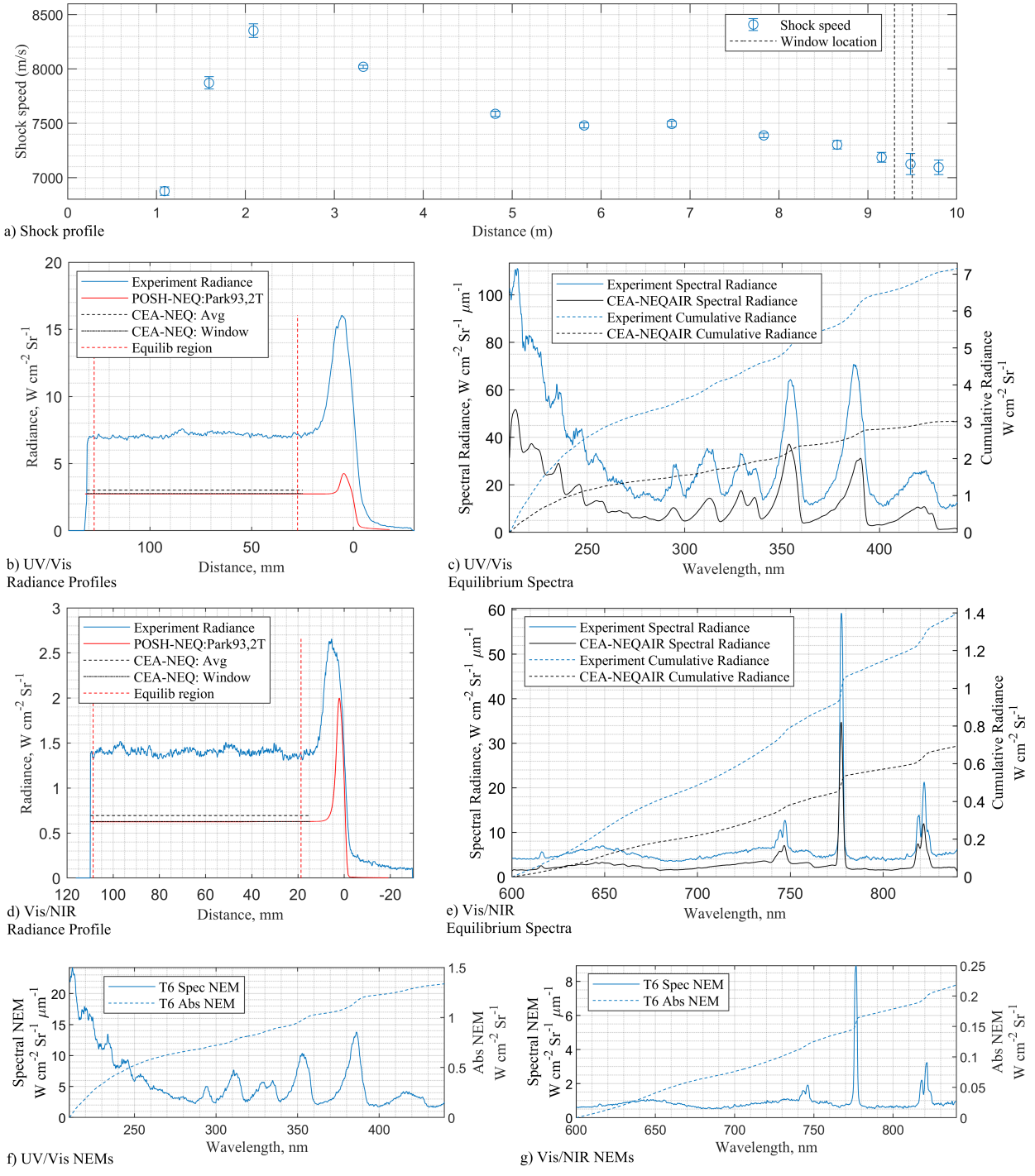

Fig. 24 Data summary for s220 at 7.21 km/s, 101 kPa post-shock pressure compared to simulations. a) shock profile; b) radiance profile and c) equilibrium spectra for UV/Vis (210-440 nm); d) radiance profile and e) equilibrium spectra for Vis/NIR (600-840 nm); measured non-equilibrium metrics for f) UV/Vis and g) Vis/NIR.

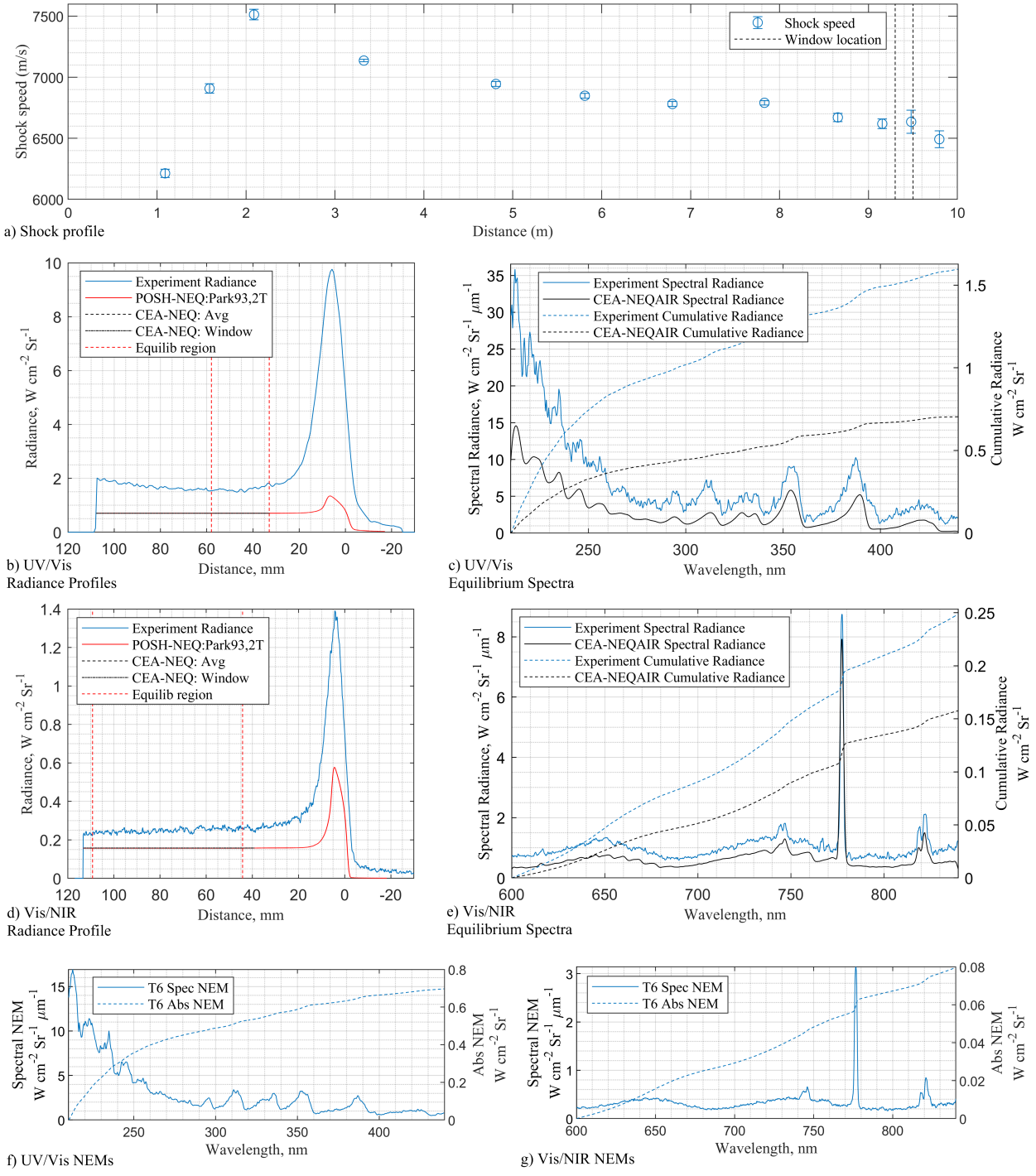

Fig. 25 Data summary for s198 at 6.64 km/s, 50 kPa post-shock pressure compared to simulations. a) shock profile; b) radiance profile and c) equilibrium spectra for UV/Vis (210-440 nm); d) radiance profile and e) equilibrium spectra for Vis/NIR (600-840 nm); measured non-equilibrium metrics for f) UV/Vis and g) Vis/NIR.

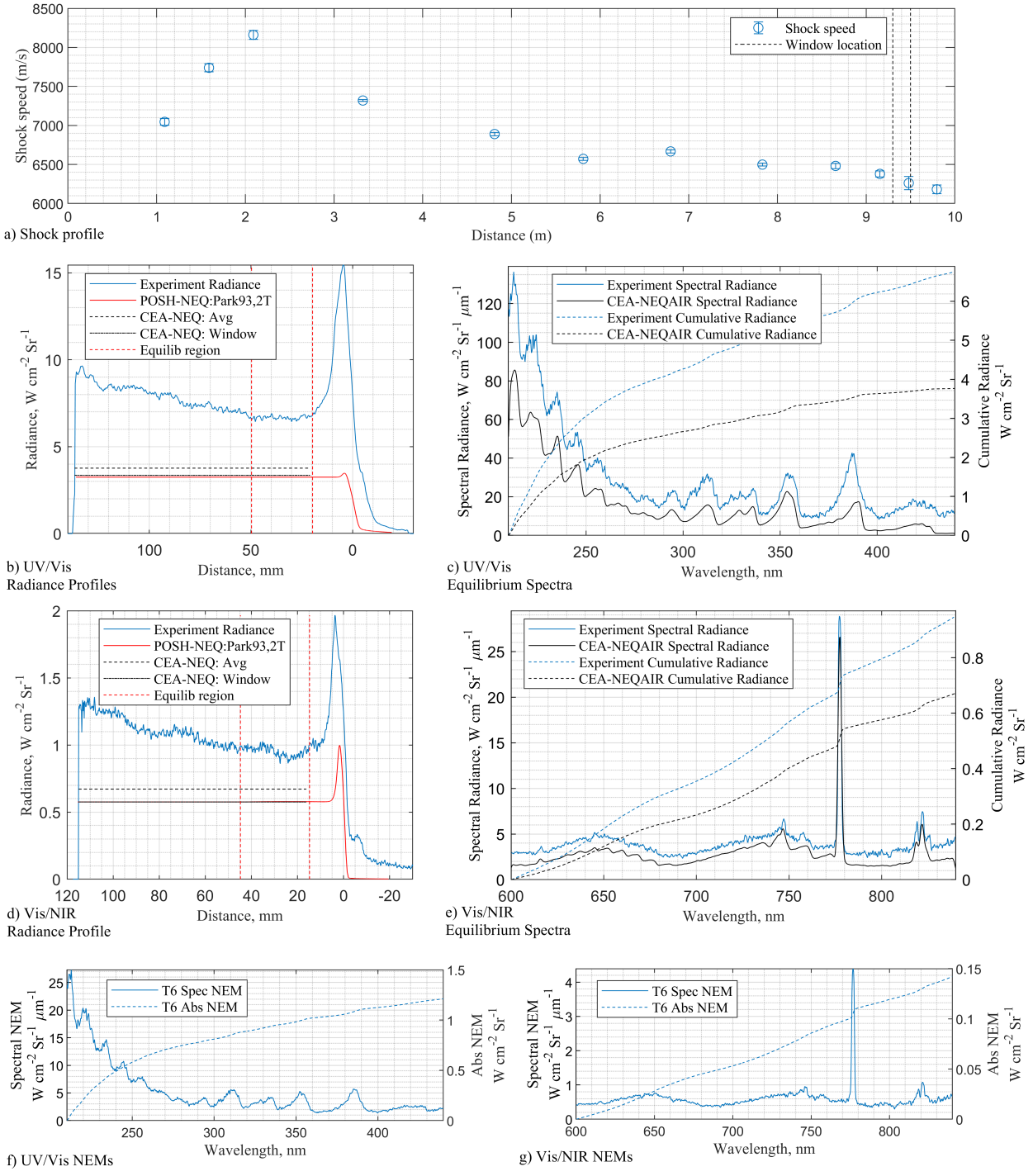

Fig. 26 Data summary for s219 at 6.37 km/s, 147 kPa post-shock pressure compared to simulations. a) shock profile; b) radiance profile and c) equilibrium spectra for UV/Vis (210-440 nm); d) radiance profile and e) equilibrium spectra for Vis/NIR (600-840 nm); measured non-equilibrium metrics for f) UV/Vis and g) Vis/NIR.

B. Equilibrium Spectra Summary

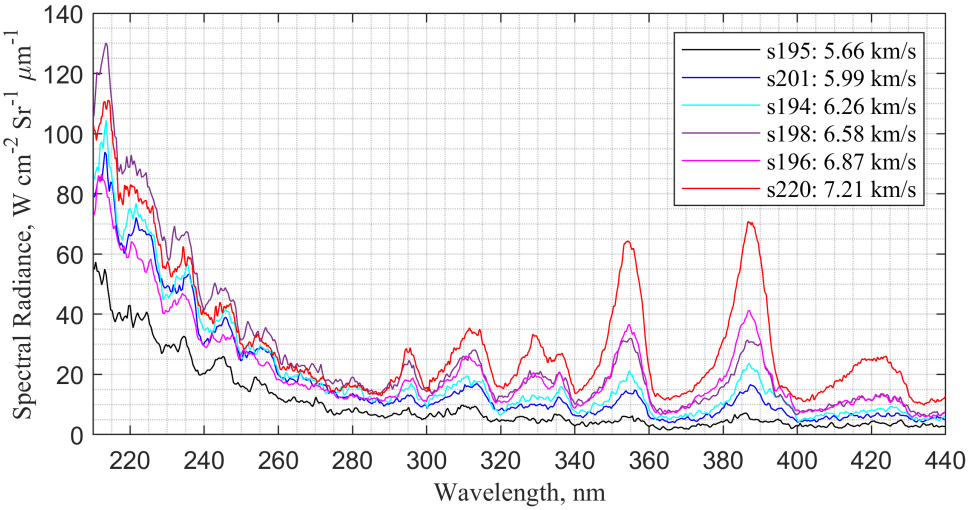

Fig. 27 Summary of spectra obtained from test cases all with 1 bar post-shock pressure in the UV/Vis region from 210-440nm.

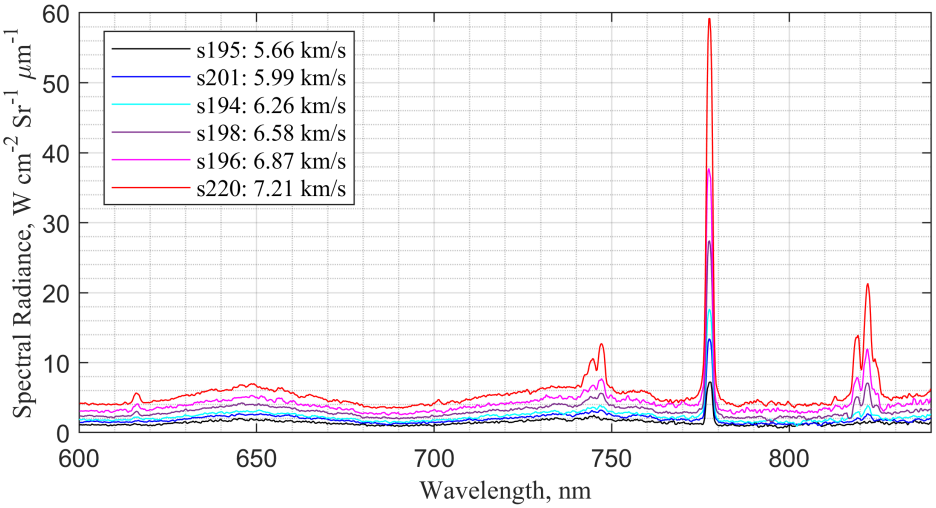

Fig. 28 Summary of spectra obtained from test cases all with 1 bar post-shock pressure in the Vis/NIR region from 600-840nm.

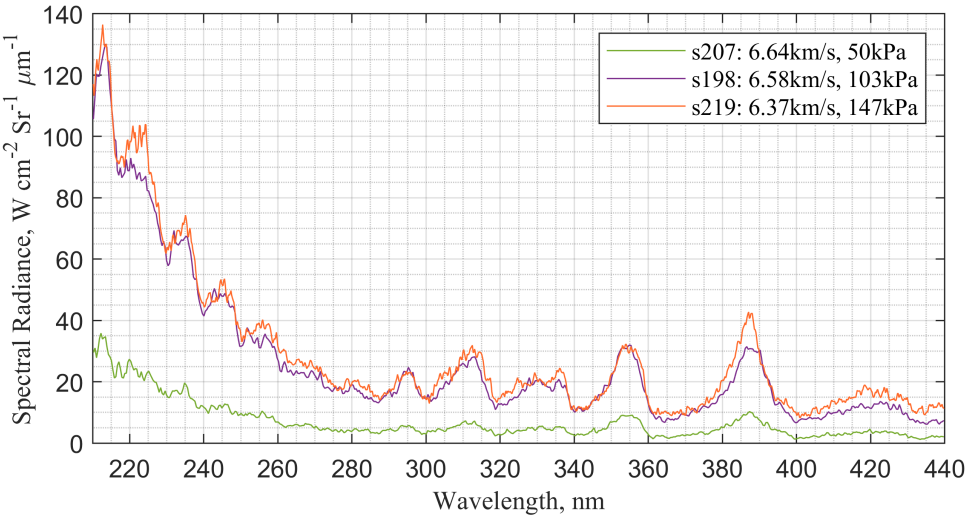

Fig. 29 Summary of spectra obtained from test cases all with 1 bar post-shock pressure in the UV/Vis region from 210-440nm.

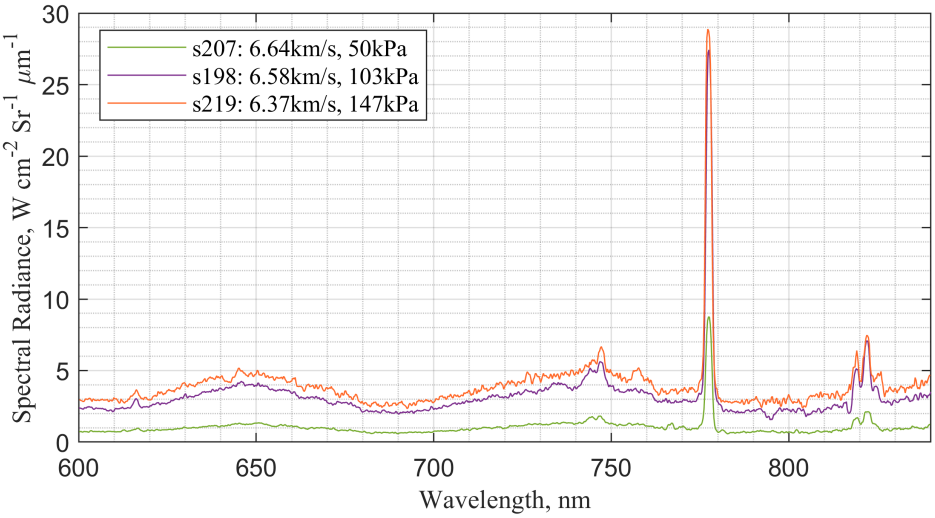

Fig. 30 Summary of spectra obtained from test cases all with similar shock speed and different post-shock pressures pressure in the Vis/NIR region from 600-840nm.

C. Radiance Profile Summary

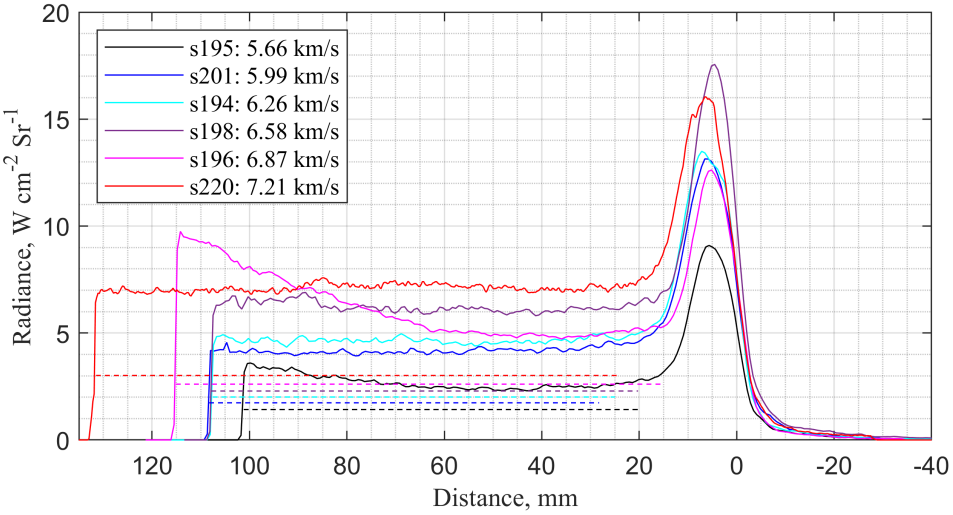

Fig. 31 Summary of radiance profiles obtained from test cases all with 1 bar post-shock pressure in the UV/Vis (210-440 nm) region. Dashed lines represent the final cumulative radiance from a CEA-NEQAIR simulation.

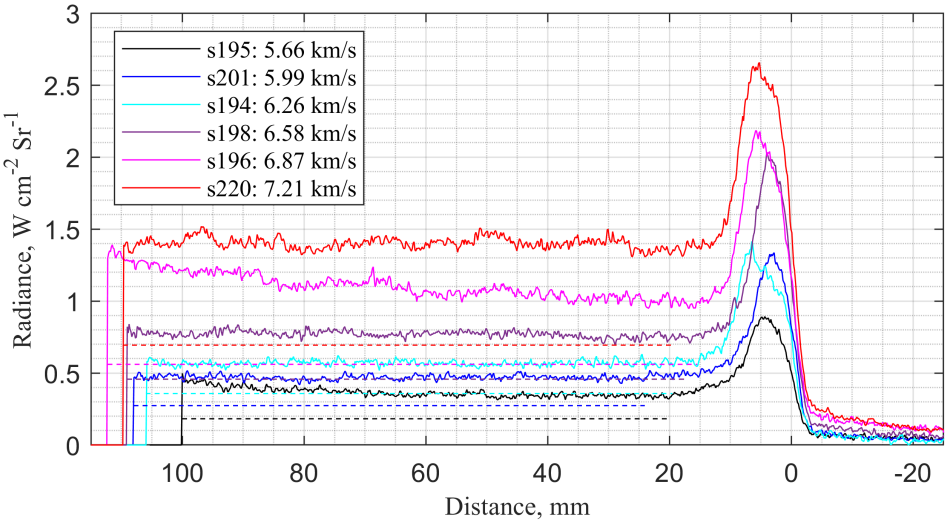

Fig. 32 Summary of radiance profiles obtained from test cases all with 1 bar post-shock pressure in the Vis/NIR (600-840 nm) region. Dashed lines represent the final cumulative radiance from a CEA-NEQAIR simulation.

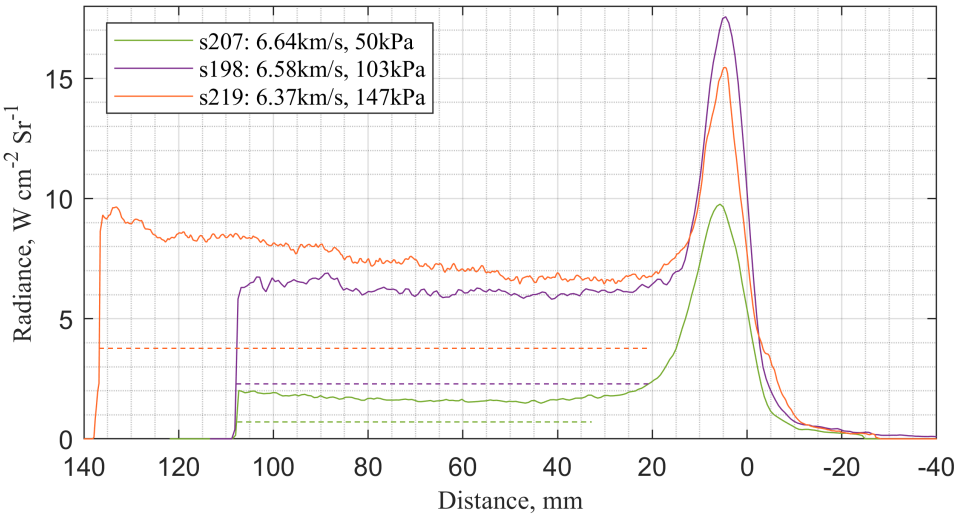

Fig. 33 Summary of radiance profiles obtained from test cases with similar shock speed and different post-shock pressure in the UV/Vis (210-440 nm) region. Dashed lines represent the final cumulative radiance from CEA-NEQAIR simulations.

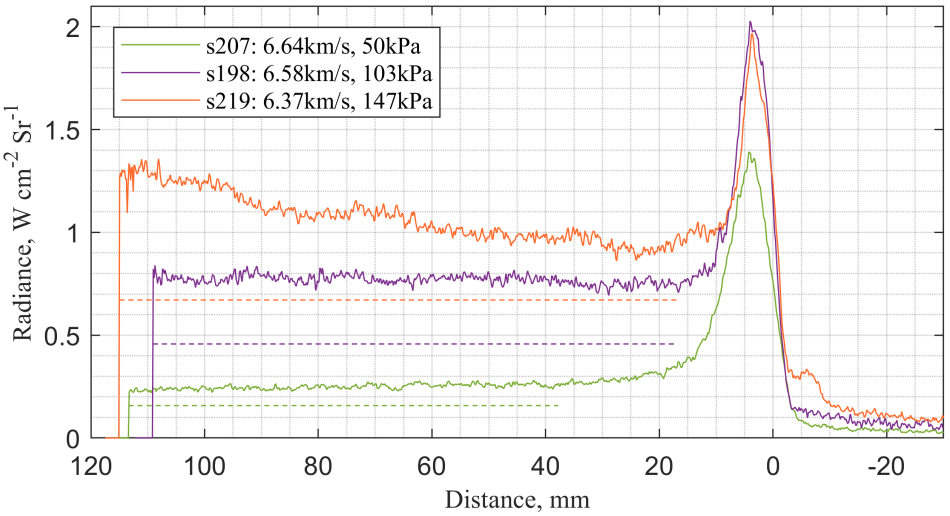

Fig. 34 Summary of radiance profiles obtained from test cases with similar shock speed and different post-shock pressure in the Vis/NIR (600-840 nm) region. Dashed lines represent the final cumulative radiance from CEA-NEQAIR simulations.

D. Spectral NEM Summaries

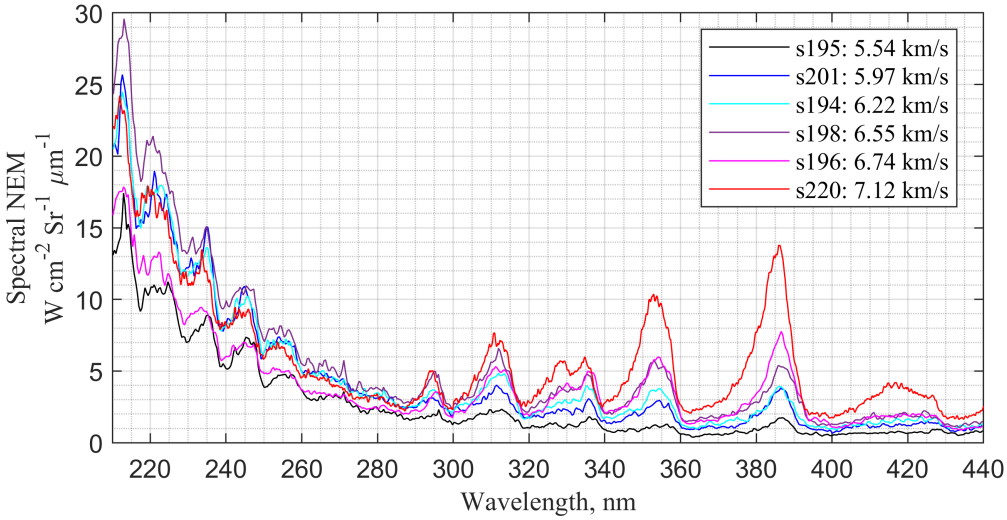

Fig. 35 Summary of spectral NEM's from the test cases with 1 bar post-shock pressure in the UV/Vis region.

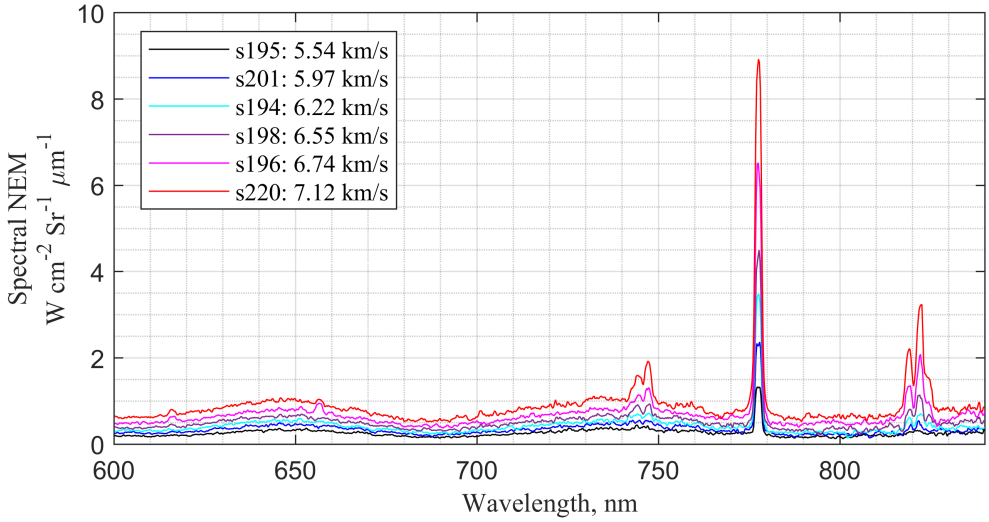

Fig. 36 Summary of spectral NEM's from the test cases with 1 bar post-shock pressure in the Vis/NIR region.

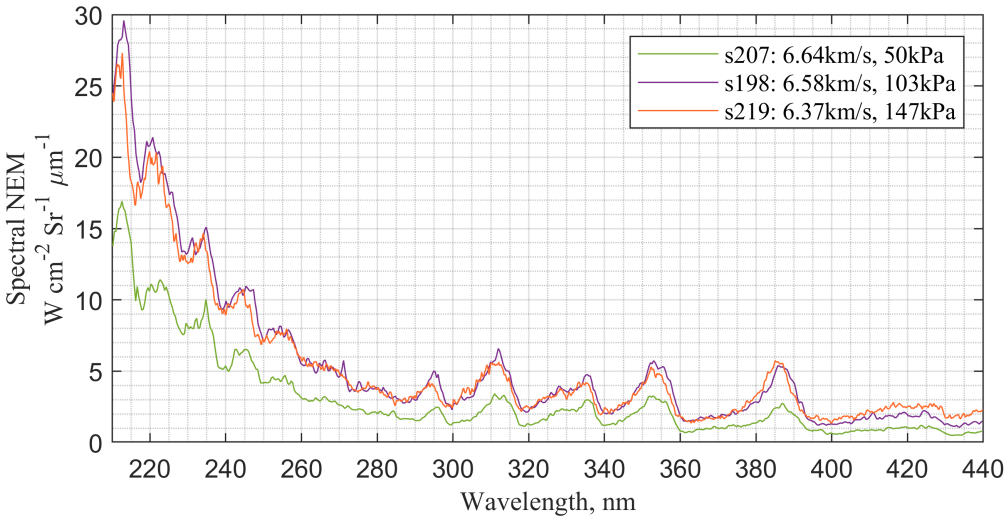

Fig. 37 Summary of spectral NEM's from the test cases with similar shock speed and different post-shock pressure in the UV/Vis region.

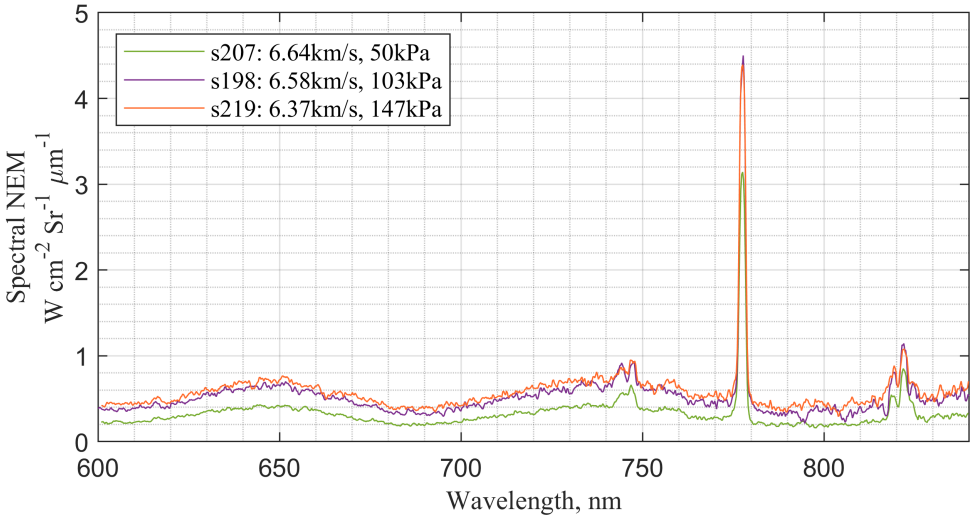

Fig. 38 Summary of spectral NEM's from the test cases with similar shock speed and different post-shock pressure in the Vis/NIR region.

Acknowledgments

The test campaign to gather data for this paper was funded by US Air Force grant FA9550-19-1-7020. The authors would like to thank Brett Cruden and Aaron Brandis at NASA Ames Research Center for their guidance on work throughout the project and for the loan of equipment, in particular the McPherson 218 spectrometer, Princeton Instruments PI-MAX2 camera and deuterium calibration lamp.

References

[1] Cruden, B. A., "Absolute radiation measurements in earth and mars entry conditions," 2014.

[2] Park, C., "Review of chemical-kinetic problems of future NASA missions. I-Earth entries," *Journal of Thermophysics and Heat transfer*, Vol. 7, No. 3, 1993, pp. 385–398.

[3] Gnoffo, P. A., Weilmuenster, K. J., Hamilton, H. H., Olynick, D. R., and Venkatapathy, E., "Computational aerothermodynamic design issues for hypersonic vehicles," *Journal of Spacecraft and Rockets*, Vol. 36, No. 1, 1999, pp. 21–43.

[4] Cruden, B. A., and Brandis, A. M., "Measurement and prediction of radiative non-equilibrium for air shocks between 7-9 km/s," 2017.

[5] Brandis, A., Johnston, C., Cruden, B., Prabhu, D., and Bose, D., "Uncertainty analysis and validation of radiation measurements for earth reentry," *Journal of Thermophysics and Heat Transfer*, Vol. 29, No. 2, 2015, pp. 209–221.

[6] Brandis, A., Johnston, C., Cruden, B., and Prabhu, D., "Equilibrium radiative heating from 9.5 to 15.5 km/s for earth atmospheric entry," *Journal of Thermophysics and Heat Transfer*, Vol. 31, No. 1, 2017, pp. 178–192.

[7] Brandis, A. M., Johnston, C. O., and Cruden, B. A., "Non-equilibrium radiation for earth entry," *46th AIAA Thermophysics Conference*, 2016, p. 3690.

[8] Collen, P., Doherty, L. J., Subiah, S. D., Sopek, T., Jahn, I., Gildfind, D., Penty Geraets, R., Gollan, R., Hambidge, C., Morgan, R., et al., "Development and commissioning of the T6 Stalker Tunnel," *Experiments in Fluids*, Vol. 62, No. 11, 2021, pp. 1–24.

[9] Collen, P., "Development of a High-Enthalpy Ground Test Facility for Shock-Layer Radiation," Ph.D. thesis, DPhil Thesis, Univ. of Oxford, Oxford, UK, 2021.

[10] Mirels, H., "Test time in low-pressure shock tubes," *The physics of Fluids*, Vol. 6, No. 9, 1963, pp. 1201–1214.

[11] James, C., Gildfind, D., Lewis, S., Morgan, R., and Zander, F., "Implementation of a state-to-state analytical framework for the calculation of expansion tube flow properties," *Shock Waves*, Vol. 28, No. 2, 2018, pp. 349–377.

[12] Collen, P., Doherty, L. J., and McGilvray, M., "Measurements of radiating hypervelocity air shock layers in the T6 free-piston driven shock tube," ESA Conference Bureau, 2019.

[13] Satchell, M., Collen, P., McGilvray, M., and Di Mare, L., "Numerical Simulation of Shock Tubes Using Shock Tracking in an Overset Formulation," *AIAA Journal*, Vol. 59, No. 6, 2021, pp. 2102–2112.

[14] Satchell, M., McGilvray, M., and Di Mare, L., "Analytical Method of Evaluating Nonuniformities in Shock Tube Flows: Theory and Development," *AIAA Journal*, 2021, pp. 1–15.

[15] Satchell, M., Glenn, A., Collen, P., Penty-Garaets, R., McGilvray, M., and di Mare, L., "An Analytical Method of Evaluating Nonuniformities in Shock Tube Flows. Part 2: Application," 2021.

[16] Satchell, M., "Numerical simulation and modeling of shock tube experiments," Ph.D. thesis, University of Oxford, 2021.

[17] Potter, D., "Modelling of radiating shock layers for atmospheric entry in Mars and Earth," Ph.D. thesis, Ph. D. Thesis, Univ. of Queensland, Brisbane, Australia, 2011.

[18] Cruden, B., "Radiance measurement for low density mars entry," *43rd AIAA Thermophysics Conference*, 2012, p. 2742.

[19] Brandis, A., Johnston, C., Panesi, M., Cruden, B., Prabhu, D., and Bose, D., "Investigation of nonequilibrium radiation for Mars entry," *51st AIAA Aerospace Sciences Meeting including the New Horizons Forum and Aerospace Exposition*, 2013, p. 1055.

[20] Huo, W. M., Liu, Y., Panesi, M., Wray, A., and Carbon, D. F., "Electron-impact excitation cross sections for modeling non-equilibrium gas," *53rd AIAA Aerospace Sciences Meeting*, 2015, p. 1896.

[21] Park, C., "Nonequilibrium Hypersonic Aerothermodynamics," 1990.